Ultra-Broadband Phase Sensitive Reflectivity Measurements of Photonic Crystals

MSc Report

L. Mulder

Supervisor: W.L. Vos, prof.dr.
Other supervisors: M.J. Goodwin, PhD, C.A.M. Harteveld, ing.
External Member: P.J.M. van der Slot, dr. (LPNO)

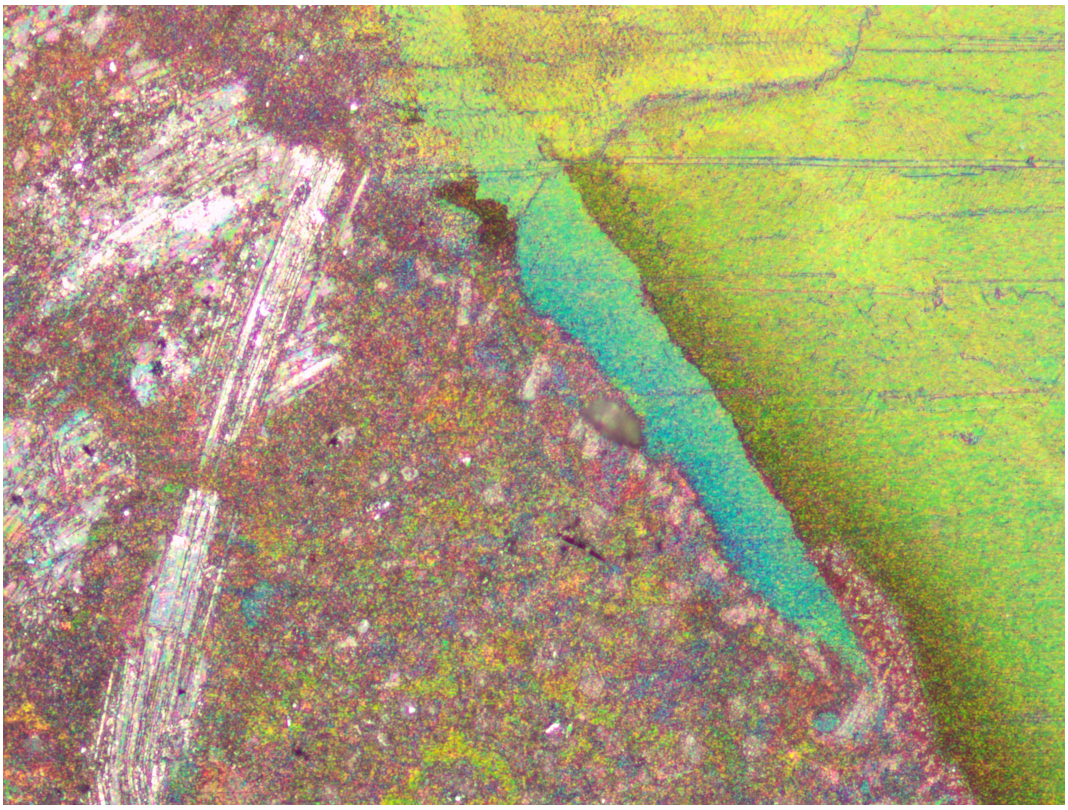

Complex Photonic Systems (COPS) Chair
MESA+ Institute
Department of Science and Technology
University of Twente, the Netherlands

August 2023

Title page: Microscope image of inverse silicon opal F113. On the right hand side there is a large, highly structured region. On the left hand side there is a region consisting of many different, small structures, which gives rise to all the different colours.

Abstract

We have built a phase sensitive white reflectivity and transmission setup based on the method designed by Kop and Sprik [1]. As innovation beyond the original proposal, we employ a supercontinuum light source since it allows for an ultra-broad band spectral bandwidth starting at 2500 nm to 900 nm. We used the pulsed nature of the supercontinuum light in combination with gated integration to increase the sensitivity and noise performance of the setup. The accuracy was verified using a measurement on a planar cavity, the results very well match our transfer matrix model. The reflection transfer functions of a number of 3D photonic and photonic bandgap crystals were studied. During these measurements we discovered a number of shortcomings with the setup which should be addressed in the future.

Acknowledgements

I want to start by thanking my supervisor Willem Vos, he came up with the fun (but very challenging) project and gave me a lot of support and freedom. Cock Harteveld, each time I had another idea or when I needed a new component, you were always ready to help, I really appreciate that. Melissa Goodwin, thank you for helping me whenever I needed some help with the samples. I want to thank Peter van der Slot for being so flexible to join in as external supervisor. I want to thank Timon Vreman for his help and advice with reflectivity measurements and for the occasional tips on which samples to measure. A lot of the scheduling of appointments was done by Nicole Meinster, thank you for helping me with this and all other administrative work. Geert Kamphuis, thank you for always assisting me trying to solve yet another problem. Plenty of times I had to lend some equipment from AQO, thank you Chris Toebes for saving me so much time by helping me out. Redlef Braamhaar, thank you for your help with RF components. Last but not least, I want to thank all other COPS members or other people that showed interested in general.

"Vele handen maken licht werk."

Contents

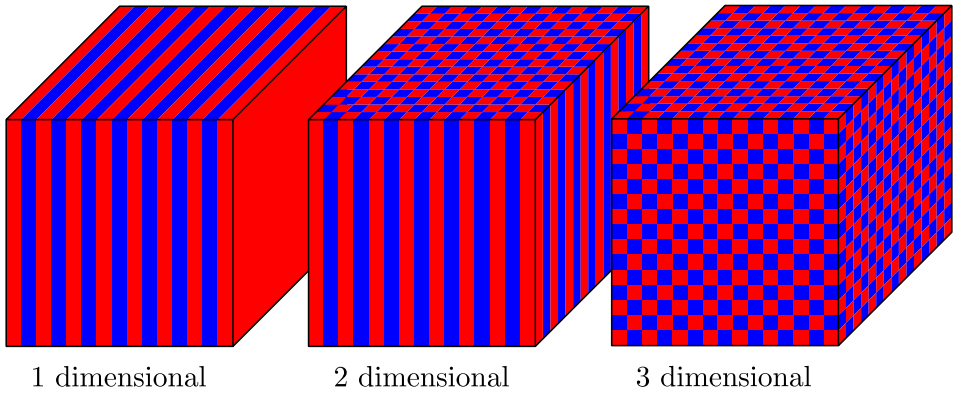

Figure 1: Cartoon to demonstrate how the dimensionality influences the structure of a photonic crystal. The red and blue colour denote two materials with a different dielectric constant.

1. Introduction

In this report we discuss the building of an ultra broadband phase sensitive reflectivity setup to measure the optical properties of photonic crystals. Photonic crystals are composite materials that have a periodically varying refractive index,[2] they can be distinguished in one-dimensional, two-dimensional and three-dimensional crystals. The dimension tells us in how many dimensions the refractive index is varying, as is demonstrated in Fig. 1. The periodic nature of photonic crystals gives rise to Bloch modes and dispersion relations for photons.[3] If the right conditions are met, this can give rise to a photonic bandgap or stop band, in a similar way how semi-conductors have electric bandgaps.[4] Photonic crystals can only confine light in the same dimensions as it has a periodicity, this means that only three-dimensional crystals can have a full photonic bandgap.

In the photonic bandgap the density of states vanishes, meaning that photons with energies in the bandgap cannot propagate in the crystal.[5] For example, this causes the forbidden light to strongly reflect from the crystal and emission of light in the bandgap will be strongly suppressed.[6,7] These interesting phenomena make the photonic bandgap an important optical property in the quest of complete control over the behaviour of light.

Due to the complex behaviour of light in photonic crystals it is difficult to understand and predict how a specific structure influences the behaviour of light. The hard work of many research groups on fabrications methods, measurements and numerical simulations have made great progress in the understanding of photonic crystals. Still, an important part of photonic crystal research is the fabrication of wide varieties of crystals and trying to correlate the measured optical properties to the geometries of the crystals. Common measured optical properties are the reflectivity, transmittance and emission control.

Reflectivity and transmittance measurements generally only take the light intensity into account, as that makes the experiments much simpler. However, the phase shift of light contains a lot of information, such as the group velocity, group velocity dispersion or group delay time. For example, at the edges of the bandgap the group velocity vanishes, while the group velocity dispersion diverges.[8]

Measuring the reflection and transmission phase shift gives us a lot of information about the properties of a photonic bandgap. For that reason the COPS chair would like to have a setup with which we cannot only measure the intensity reflection or transmission, but also the phase shift. In this project we build such a setup and verify its proper functioning. We have done a number of measurements on interesting photonic crystals. The crystals we measured are a Bragg stack with defect, an inverse $\sqrt{2}$ crystal, a direct woodpile crystal, an inverse woodpile crystal, a polystyrene opal and an inverse silicon opal.

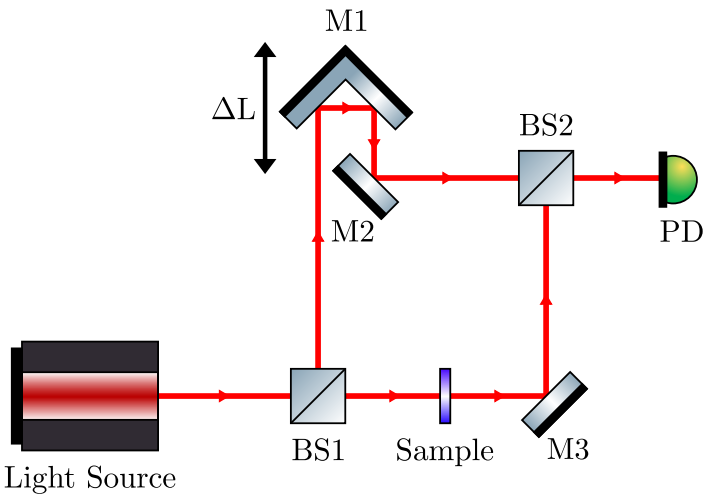

Figure 2: Schematic of a typical transmission cross-correlation setup based on a Mach-Zehnder interferometer. The setup contains two beamsplitters (BS), three mirrors (M), a light source and a photodiode (PD). By measuring the PD signal for multiple path length differences ΔL we can determine the cross-correlation of the reference field and the field influenced by a sample. This allows us to directly measure the complete field transmission transfer function of the sample.

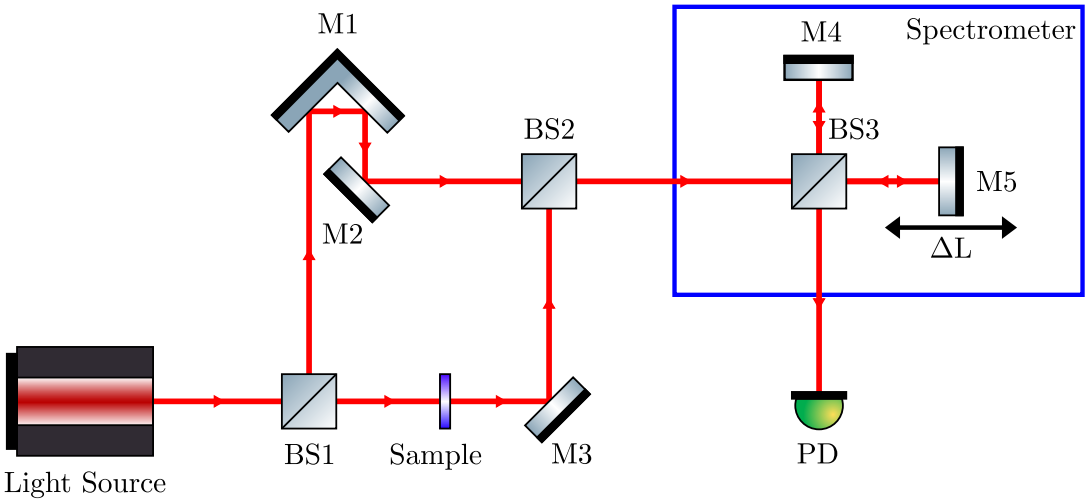

Figure 3: Schematic of an alternative transmission cross-correlation setup consisting of a Mach-Zehnder interferometer combined with a Michelson interferometer. The setup contains three beamsplitters (BS), five mirrors (M), a light source and a photodiode (PD). Part of the components are contained in a commercially available spectrometer.

2. Phase Resolved Interferometry

2.1 Introduction to Phase Resolved Interferometry

A common application of phase resolved interferometry is the measurement of group velocity dispersion in materials.[9,10] In order to measure the group velocity dispersion we need to measure the complex transmission transfer function of a sample. A transfer function describes how the individual frequency components of the electric field are influenced by a sample. In the case of a transmission transfer function it tells us the change of the field amplitude and the phase shift caused by propagation through the sample. The group velocity dispersion is calculated from the phase information of the transfer function.

Such transfer function measurements can be done with a cross-correlation setup as in Fig. 2, where we take the cross-correlation between a sample field and a reference field. On the photodiode we then measure an intensity depending on a time delay:

$$I_{\mathrm{PD}}(\tau) = \mathrm{Const.} + \mathrm{Re}\left\{\mathcal{F}\left\{I_{\mathrm{ls}}(\omega)H_{\mathrm{sam}}(\omega)H^*_{\mathrm{ref}}(\omega)\right\}(\tau)\right\} \tag{1}$$

Here $I_{\mathrm{ls}}(\omega)$ is the intensity spectrum of the light source, $H_{\mathrm{sam}}(\omega)$ the transfer function of the sample arm, $H_{\mathrm{ref}}(\omega)$ the transfer function of the reference arm and τ a variable time-delay between the sample and reference arm due to an adjustable path-length difference ΔL. By measuring the intensity for a range of path-length differences ΔL and converting the measurements to the frequency domain using a Fourier transform we determine the transmission transfer function of a sample. For accurate measurements we need the path length difference between the two arms of the interferometer to be set with nanometre accuracy. This is difficult to accomplish in a home-build setup, but we can easily mitigate this problem by using a commercially available Fourier transform spectrometer. For example, COPS has a Bio-Rad FTS6000 spectrometer, which can change the path length difference between the arms of its interferometer accurately with step sizes of about 80 nm. Unfortunately, due to the way such a spectrometer is build we cannot place a sample in one of the arms.

There is an easy way to solve this problem using an alternative setup designed by Kop and Sprik[1], shown in Fig. 3. Here we still have the Mach-Zehnder interferometer, but we keep the path length difference constant and place a Fourier transform spectrometer at the output of the Mach-Zehnder interferometer. The spectrometer consists of a Michelson interferometer and will then take the auto-correlation of the sum of the reference and sample fields, which also contains the cross-correlation of the reference and sample field. On the photodiode we then measure the intensity:

$$\begin{aligned} I_{\mathrm{PD}}(\tau) = {} & \mathrm{Const.} + \mathrm{Re}\left\{\mathcal{F}\left\{I_{\mathrm{ls}}(\omega)H_{\mathrm{sam}}(\omega)H^*_{\mathrm{ref}}(\omega)\right\}(\tau)\right\} \\ & + \mathcal{F}\left\{I_{\mathrm{ls}}(\omega)\left|H_{\mathrm{sam}}(\omega)\right|^2\right\}(\tau) + \mathcal{F}\left\{I_{\mathrm{ls}}(\omega)\left|H_{\mathrm{ref}}(\omega)\right|^2\right\}(\tau) \end{aligned} \tag{2}$$

Compared to Eq. 1 we now have two extra terms that only contain the amplitude information of respectively the sample and reference arm transfer functions. By doing two additional measurements where we close either the sample or reference arm we extract the desired cross-correlation term.

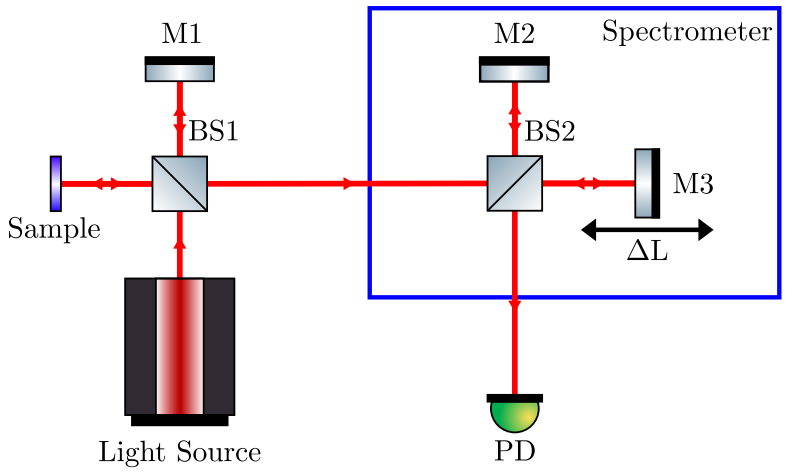

Figure 4: Schematic of a cross-correlation setup for reflectivity measurements. It uses a Michelson interferometer instead of a Mach-Zehnder interferometer. The setup contains two beamsplitters (BS), three mirrors (M), a light source and a photodiode (PD). Part of the components are contained in a commercially available spectrometer.

2.2 Proposition for the Measurement Method

The aforementioned measurement method from Kop and Sprik[1] has been shown before to be very suitable for measuring the group velocity and group velocity dispersion. However, there are a number of changes we can make that change the abilities and ease of use of the setup.

First of all, we choose to use a different light source. Previous COPS studies have often used a femtosecond pulsed Ti:Sa laser that can be tuned to wavelengths ranging from 750 nm to 850 nm with a bandwidth (FWHM) of around 10 nm. The output power is generally more than a watt, so that impressive signal to noise ratios are possible. Unfortunately, most available samples are designed to have a bandgap, or other regions of interest, outside this spectral range. This means that we either have to make some new samples, which is often very tedious, or we have to use a different light source.

Here we propose to use a new light source, specifically a supercontinuum white light source. The supercontinuum source available to us has an ultra-broad spectrum ranging from around 450 nm to 2400 nm with a total output power of a hundred milliwatt. The advantage of this is that this would allow us to measure a huge spectral range and thus all existing available samples. The disadvantage is that we now have a lower spectral power density of tens of microwatts per nanometre opposed to the hundreds of milliwatts per nanometre with the Ti:Sa laser. From experience we know that the signal to noise ratios even with these lower spectral power densities are still more than acceptable, so that the advantages outweigh the disadvantages.

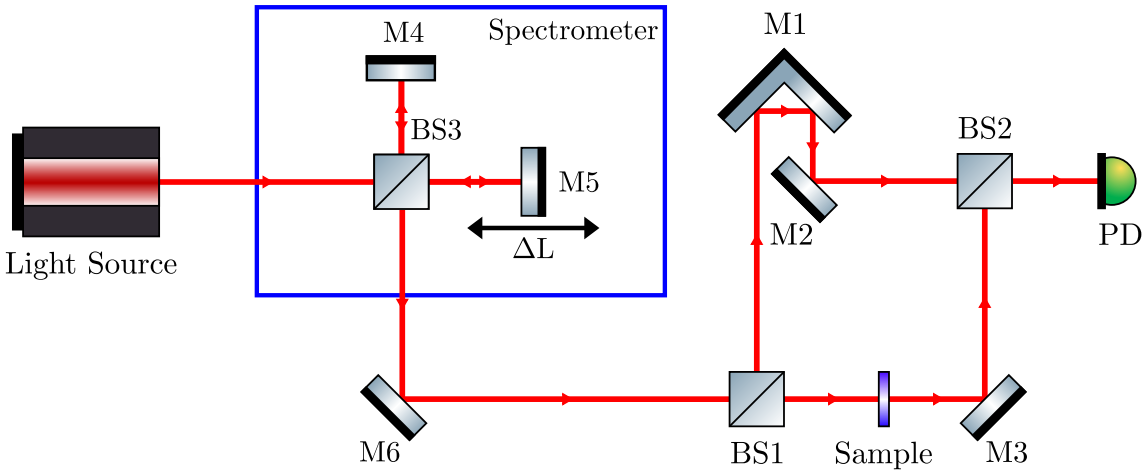

Figure 5: Schematic of an alternative transmission cross-correlation setup. Here we have placed the Fourier transform spectrometer before the Mach-Zehnder interferometer. The setup contains three beamsplitters (BS), five mirrors (M), a light source and a photodiode (PD). Part of the components are contained in a commercially available spectrometer.

Secondly, the samples we plan to measure require another change. Due to the geometry of these samples transmission measurements are not always possible. Hence we are constrained to reflectivity geometry. This means that when in Fig. 3 the sample is located in a Mach-Zehnder interferometer for the transmission measurements, we have to place the sample in a Michelson interferometer for reflectivity measurements, as is shown in Fig. 4. In this way we cannot measure group velocity dispersion, but we can measure a reflection time delay.

Thirdly, instead of using a Fourier transform spectrometer, we could also use any other type of spectrometer. This is because we can simply transform from a cross-correlation in time to a frequency spectrum and back via a Fourier transform. We could for instance decide to use a compact grating spectrometer, this would save a lot of space and make the setup simpler. There are a number of reasons why we want to stick with the Fourier transform spectrometer.

Other types of spectrometers often only measure a very limited spectral range. This makes it much harder to accurately reconstruct the original field cross-correlation. The availability of resources is also an important consideration. Currently, COPS has three Fourier transform spectrometers and a few IR monochromators available, but no compact NIR spectrometer. This means that we either have to wait until new spectrometers arrive, or we use one of the available Fourier transform spectrometers that are slightly harder to use experimentally, but give easier to use measurement data. We decide in favour of the last option.

Fourthly, since we are working with linear optical systems that fulfil time-reversal symmetry, there is in principle no difference in either placing the Fourier transform spectrometer before the Mach-Zehnder interferometer or after the interferometer. A design with the spectrometer before the Mach-Zehnder interferometer is shown in Fig. 5. This way we interpret the combination of the supercontinuum source and the spectrometer as a tunable light source that allows us to set the spectral Fourier component.

We then use the modulated light in any optical circuit we want and only have to add a photodiode at the end of the circuit. This has the advantage that alignment becomes easier, if we change the sample, or even redirect the light to a different optical circuit, we have to realign far fewer parts and we don't have to worry about the somewhat complex light path through the spectrometer. There is of course also a disadvantage to this method, the Bio-Rad spectrometer has a number of moving mirrors in the optical path. Before we do measurements we thus have to make sure that the beam leaving the Bio-Rad spectrometer still has sufficient pointing stability for microscopy.

Fifth, it is important that we have a high signal to noise ratio in order to accurately determine the transfer function of our samples. We could repeat the same measurement many times N and take the average of all results, but random noise power only slowly decreases with a factor $\sqrt{N}$. There is a practical limit to the measurement time, so there is also a practical limit to the reduction in noise with this method. Furthermore, this method will not get rid of background signals, as those do not have a random phase. This means that we will also have to do a background measurement. A better approach would be to minimise the noise before the signals are even measured.

There are a number of ways that this is generally done. First of all, we should remove as many noise sources as possible. For example, this is done using shielding to reduce any stray light or air turbulence. We also want to use a damped optical table to minimise vibration. After we have eliminated all possible noise sources we can resort to filtering noise using knowledge we have about the signal.

Two methods are available that can reduce noise in measurements. The first method filters noise using frequency information about the measured signal. This is accomplished using a lock-in detector that is synchronised to either the pulse repetition rate of the supercontinuum source or to an external modulator such as a chopper.[11] The second method uses the time information about the measured signal. A gated integrator uses the pulsed nature of the supercontinuum light, generally a few nanoseconds pulse width, to only measure during the pulse and so reject most of the noise. The noise rejection then depends on the pulse width and the number of pulses per seconds. We will further discuss this in section 3.4.

2.3 Mathematical Description of Phase Resolved Interferometry

In this section we give a mathematical description how measurements with a cross-correlate setup, as shown in Fig. 5, are used to determine the transmission or reflection transfer function of a sample. We will describe the individual parts of the setup in terms of transfer functions. There are two transfer functions for the two interferometers, all other components such as mirrors and filters will be summarised by a system transfer function H_{sys}.

Fourier transform spectrometers consist of a Michelson interferometer with two similar arms H_1 and H_2. The optical path length of one arm is changed to give an adjustable time delay τ, in frequency space this is equal to a multiplication with $e^{i\omega\tau}$. The transfer function for a Fourier transform spectrometer is thus:

$$H_{\mathrm{FTS}}(\omega,\tau) \equiv H_1(\omega) + H_2(\omega)e^{i\omega\tau} \tag{3}$$

The next part of the experimental setup is a secondary interferometer. For transmission measurements this can be a Mach-Zehnder interferometer and for reflection measurements a Michelson interferometer. In principle it does not matter what type of interferometer is used, as long as it has two arms H_3 and H_4. Arm H_4 contains a sample. The transfer function for an arbitrary stationary interferometer is thus:

$$H_{\mathrm{int}}(\omega) \equiv H_3(\omega) + H_4(\omega)H_{\mathrm{sam}}(\omega) \tag{4}$$

On the photodiode at the output the light field E_{PD} depends on the field E_{ls} coming from the light source and on the three transfer functions H_{sys}, H_{FTS} and H_{int}. It is given by:

$$E_{\mathrm{PD}}(\omega,\tau) \equiv E_{\mathrm{ls}}(\omega)H_{\mathrm{sys}}(\omega)H_{\mathrm{FTS}}(\omega,\tau)H_{\mathrm{int}}(\omega) \tag{5}$$

The photodiode measures the average optical power as a function of the time delay τ. Furthermore, the photodiode has a responsivity R_{PD}. The average optical power P_{both} measured by the photodiode when both arms are open is thus the product of the responsivity and the squared absolute field integrated over all light frequencies.

$$\begin{aligned} P_{\mathrm{both}}(\tau) &= \int_{-\infty}^{\infty} R_{\mathrm{PD}}(\omega,\tau)|E_{\mathrm{PD}}(\omega)|^2 \mathrm{d}\omega \\ &= \int_{-\infty}^{\infty} R_{\mathrm{PD}}(\omega)|E_{\mathrm{ls}}(\omega)H_{\mathrm{sys}}(\omega)H_{\mathrm{FTS}}(\omega,\tau)H_{\mathrm{int}}(\omega)|^2 \mathrm{d}\omega \end{aligned} \tag{6}$$

The previous equation can be written as a combination of all field transfer functions:

$$\begin{aligned} P_{\mathrm{both}}(\tau) = &\int_{-\infty}^{\infty} R_{\mathrm{PD}}(\omega)\left|E_{\mathrm{ls}}(\omega)H_{\mathrm{sys}}(\omega)\right|^2 \\ &\times \left(|H_3(\omega)|^2 + |H_4(\omega)|^2 |H_{\mathrm{sam}}(\omega)|^2 + 2\,\mathrm{Re}\left\{H_3^*(\omega)H_4(\omega)H_{\mathrm{sam}}(\omega)\right\}\right) \\ &\times \left(|H_1(\omega)|^2 + |H_2(\omega)|^2 + 2\mathrm{Re}\left\{H_1^*(\omega)H_2(\omega)e^{i\omega\tau}\right\}\right) \mathrm{d}\omega \end{aligned} \tag{7}$$

Several terms of the integral are independent of the time delay τ, namely $|H_1|^2$ and $|H_2|^2$. These give a constant offset, so we simplify the integral to:

$$\begin{aligned} P_{\mathrm{both}}(\tau) = &\ \mathrm{Const} + 2\int_{-\infty}^{\infty} R_{\mathrm{PD}}(\omega)\left|E_{\mathrm{ls}}(\omega)H_{\mathrm{sys}}(\omega)\right|^2 \times \\ &\left(|H_3(\omega)|^2 + |H_4(\omega)|^2 |H_{\mathrm{sam}}(\omega)|^2 + 2\,\mathrm{Re}\left\{H_3^*(\omega)H_4(\omega)H_{\mathrm{sam}}(\omega)\right\}\right) \times \\ &\mathrm{Re}\left\{H_1^*(\omega)H_2(\omega)e^{i\omega\tau}\right\} \mathrm{d}\omega \end{aligned} \tag{8}$$

All individual terms in the integral are real, so we can further simplify this to:

$$\begin{aligned} P_{\text{both}}(\tau) = \text{ Const} + 2\,\text{Re}\Bigg\{ \int_{-\infty}^{\infty} R_{\text{PD}}(\omega)\left|E_{\text{ls}}(\omega)H_{\text{sys}}(\omega)\right|^2 H_1^*(\omega)H_2(\omega)\times \\ \left(\left|H_3(\omega)\right|^2 + \left|H_4(\omega)\right|^2\left|H_{\text{sam}}(\omega)\right|^2 + 2\,\text{Re}\left\{H_3^*(\omega)H_4(\omega)H_{\text{sam}}(\omega)\right\}\right) e^{i\omega\tau}\text{d}\omega \Bigg\} \end{aligned} \tag{9}$$

Next, we define a system term A_{sys} as:

$$A_{\text{sys}}(\omega) \equiv R_{\text{PD}}(\omega)\left|E_{\text{ls}}(\omega)H_{\text{sys}}(\omega)\right|^2 H_1^*(\omega)H_2(\omega) \tag{10}$$

This term simplifies Eq. 9 to:

$$\begin{aligned} P_{\text{both}}(\tau) = \text{ Const} + 2\,\text{Re}\Bigg\{ \int_{-\infty}^{\infty} A_{\text{sys}}(\omega)\times \\ \left(\left|H_3(\omega)\right|^2 + \left|H_4(\omega)\right|^2\left|H_{\text{sam}}(\omega)\right|^2 + 2\,\text{Re}\left\{H_3^*(\omega)H_4(\omega)H_{\text{sam}}(\omega)\right\}\right) e^{i\omega\tau}\text{d}\omega \Bigg\} \end{aligned} \tag{11}$$

We recognize that the integral is nothing but an inverse Fourier transform.

$$\begin{aligned} P_{\text{both}}(\tau) = \text{ Const} + 2\,\text{Re}\left\{\mathcal{F}_{\omega\to\tau}\left\{A_{\text{sys}}(\omega)\times \right.\right. \\ \left.\left.\left(\left|H_3(\omega)\right|^2 + \left|H_4(\omega)\right|^2\left|H_{\text{sam}}(\omega)\right|^2 + 2\,\text{Re}\left\{H_3^*(\omega)H_4(\omega)H_{\text{sam}}(\omega)\right\}\right)\right\}\right\} \end{aligned} \tag{12}$$

The Kramers-Kronig relations[12,13] directly relate the imaginary part of this inverse Fourier transform to the real part. A convenient way of implementing the Kramers-Kronig relations is by multiplication with the step-function in the time domain.[14] This means that from Eq. 11 we can determine:

$$\tilde{P}_{\text{both}}(\omega) = A_{\text{sys}}(\omega)\left(\left|H_3(\omega)\right|^2 + \left|H_4(\omega)\right|^2\left|H_{\text{sam}}(\omega)\right|^2 + 2\,\text{Re}\left\{H_3^*(\omega)H_4(\omega)H_{\text{sam}}(\omega)\right\}\right) \tag{13}$$

We do two more measurements with each either arm H_3 or arm H_4 closed. This is expressed by setting the transfer functions of either arm to zero, which according to Eq. 13 gives:

$$\tilde{P}_3(\omega) = A_{\text{sys}}(\omega)\left|H_3(\omega)\right|^2 \tag{14}$$

$$\tilde{P}_4(\omega) = A_{\text{sys}}(\omega)\left|H_4(\omega)\right|^2\left|H_{\text{sam}}(\omega)\right|^2 \tag{15}$$

Using the previous three measurements we then determine the real part of the uncalibrated sample transfer function to be:

$$\begin{aligned} \text{Re}\left\{H_{\times,\text{sam}}(\omega)\right\} &= \frac{\tilde{P}_{\text{both}}(\omega) - \tilde{P}_3(\omega) - \tilde{P}_4(\omega)}{\tilde{P}_3(\omega)} \\ &= 2\,\text{Re}\left\{\frac{H_4(\omega)}{H_3(\omega)}H_{\text{sam}}(\omega)\right\} \end{aligned} \tag{16}$$

The imaginary part of Eq. 16 can be determined using the Kramers-Kronig relations. We repeat the three measurements, but now we replace the sample with a reference to calibrate the setup. In case of a transmission measurement this is often simply air and in case of reflection this is often a gold mirror. This gives us the calibration transfer function:

$$H_{\times,\mathrm{cal}}(\omega) = \frac{2H_4(\omega)}{H_3(\omega)} H_{\mathrm{ref}}(\omega) \tag{17}$$

Combining Eq. 16 and Eq. 17 we get the final, calibrated sample transfer function.

$$\begin{aligned} H_{\times}(\omega) &= \frac{H_{\times,\mathrm{sam}}(\omega)}{H_{\times,\mathrm{cal}}(\omega)} \\ &= \frac{H_{\mathrm{sam}}(\omega)}{H_{\mathrm{ref}}(\omega)} \end{aligned} \tag{18}$$

To measure the transfer function of a sample we thus have to do three measurements for the sample and three measurements for a calibration. There are no system dependent parts anymore in Eq. 16 and Eq. 17, so as long as the second interferometer remains unchanged, the calibration measurements also remains valid even when for example the light source is fluctuating over time.

2.4 Error Analysis

Each measurement $\tilde{P}_i$ is averaged over a large number of individual scans to reduce noise. We can estimate the error in our measurements by doing a statistical analysis of the scans. For this we will assume that the errors among the individual scans are caused due to random normal distributed noise with mean zero. These assumptions will be validated in section 3.4.1.

For each individual scan we determine $\tilde{P}_{\mathrm{both}}$, $\tilde{P}_3$ and $\tilde{P}_4$ respectively as described in section 2.3 and we take the average. We also determine the standard deviation so that we know $\delta\tilde{P}_{\mathrm{both}}$, $\delta\tilde{P}_3$ and $\delta\tilde{P}_4$ respectively. Using the standard deviation of the measurements we want to determine the error in $|H_{\times}|^2$ and $\arg\{H_{\times}\}$. This can be done using statistical error propagation. In the case of independent variables the error propagation is given by:[15]

$$(\delta g(x_1, x_2, \dots))^2 = \sum_i \left(\frac{\partial g(x_1, x_2, \dots)}{\partial x_i} \right)^2 (\delta x_i)^2 \tag{19}$$

Unfortunately, we have to combine six complex valued variables, which leads to long and complex error relations. For that reason we decided to not include the derivation in the report, but it is available on request.

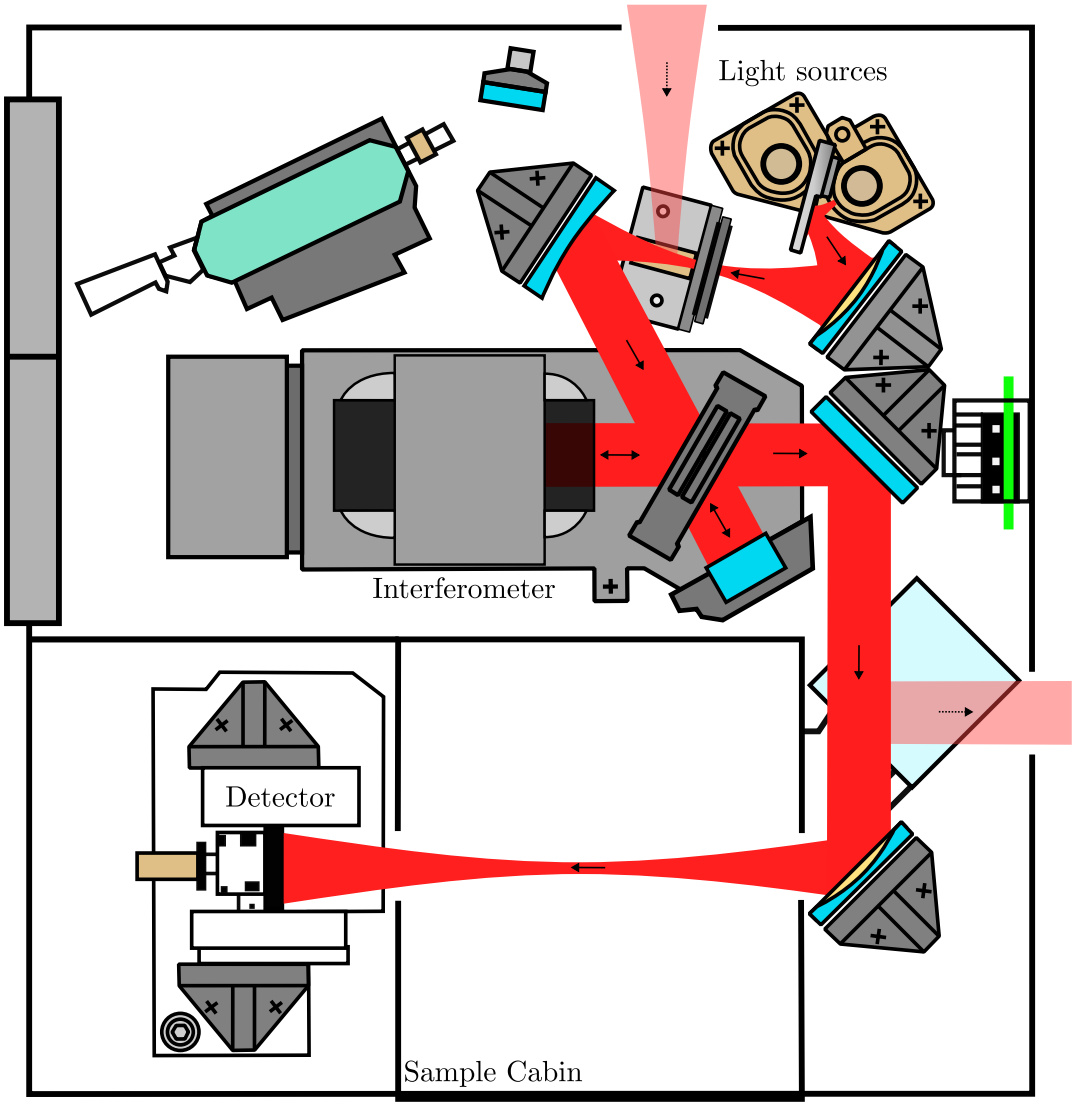

Figure 6: Schematic of the Bio-Rad FTS6000 Fourier transform spectrometer. All mirrors are coloured cyan. The spectrometer is meant to be used with internal light sources and an internal detector. The red beams show how the light propagates from the light sources, through the interferometer and sample cabin, to the detector. However, the spectrometer does support the use of an external light source mounted to the entrance at the top and has a number of accessories that can be attached to the output at the right side of the device. We exploit the entrance and output ports for our experiments. The schematic was made with help of the Bio-Rad FTS6000 manual.

3. Realisation of a Phase Sensitive Reflectivity Setup

The experimental setup can be divided in a number of functional blocks. We start with the Fourier modulated light source. The resulting light can then be routed to either a reflection or transmission optical circuit. Finally, the light is measured using a pulse detection scheme. In the following sections these functional blocks will be discussed.

3.1 Fourier modulated light source

The first step is to build a Fourier modulated light source. As a light source we use a supercontinuum source (SuperK Compact, NKT Photonics). The source has a total output power of at least 110 mW at a repetition rate of 20 kHz and has a spectral range from 450 nm to 2400 nm. We specifically need a supercontinuum source, as it produces spatial single mode light. This allows us to focus all of the light into a very small spot, only limited by our choice of focal system and the diffraction limit. Spatially resolved spectroscopy, even with microscopic samples, is then possible. An incandescent light source such as a halogen bulb would be unsuitable for this, as the focus size would often be larger than the sample.

To modulate the light we use interferometer of the Bio-Rad FTS6000 spectrometer. A schematic of the spectrometer is shown in Fig. 6. The interferometer splits the single light beam into two spatially overlapping beams between which a precise time delay can be set. The mathematics behind this have been discussed before in section 2.3.

An important step is conditioning the supercontinuum light. First we use a continuously variable ND filter (NDC-50C-2M, Thorlabs) to tune the light power going to the optical circuits. Then we use a beam-expander (BE04R, Thorlabs) to increase the beam-width. Increasing the beam-width helps to decrease the divergence of the light beam. Furthermore, the spectrum of the light coming from the supercontinuum source still contains a large, sharp peak from the pump laser in the supercontinuum source. It turns out that this pump peak is mostly circularly polarised, while the rest of the supercontinuum light is unpolarised. We thus use a quarter-wave plate and a polarizer (WP25M-UB, Thorlabs) to filter out most of the pump light. This polarizer is also used to set the wanted polarisation of the light.

A movable mirror is used to select either the supercontinuum light or the light from a Helium Neon laser for the subsequent optical circuits. The coherent HeNe light allows us to see interference fringes, this aids the alignment of interferometers.

3.1.1 Spectrometer Hardware Upgrade

We want to upgrade the hardware of the spectrometer, because we want to use the device differently than it is designed for. Normally, the device is entirely self-contained with the possibility of adding some external accessories. One of the accessories is an external light source, due to the way the device is made this incoming light has to be converging. A toroidal

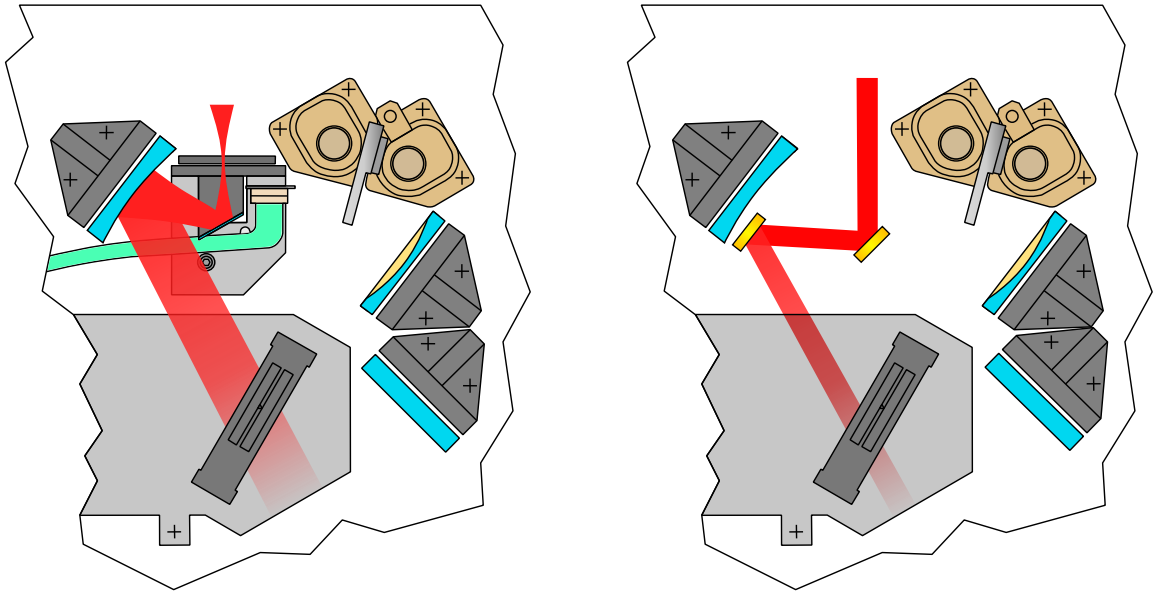

(a) Old layout **(b)** New layout

Figure 7: **(a)** Old layout: The incoming light has to be focused through a diaphragm and indirectly onto a toroidal mirror. The toroidal mirror collimates the light and injects it into the Michelson interferometer of the spectrometer. **(b)** New layout: We place a small 1" mirror in front of the toroidal mirror and avoid the diaphragm. This makes it much easier to align the setup.

mirror in the device then collimates the light beam after which it is injected into a Michelson interferometer, this is highlighted in Fig. 7a. Normally this would not be a problem, as the external light source would be aligned in factory. We use a completely different kind of light source the spectrometer is not designed for, a supercontinuum light source.

Previously, an off-axis parabolic mirror was used to converge the supercontinuum light beam. The alignment of this is very hard, as we have to make sure that we use the right focal distance and hit the correct spot of the toroidal mirror while we aim the beam through a small diaphragm. Due to the combination of a parabolic mirror and a toroidal mirror it is impossible to get a nicely collimated beam with any beam quality. To fix this we have completely circumvented the toroidal mirror by placing a small flat mirror in front of it and we changed the module with the diaphragm and mirror to a single flat mirror. The external parabolic mirror is then not necessary anymore. The new layout is shown in Fig. 7b. Our supercontinuum light beam has a diameter of about 3 mm, which is much smaller than the light beam of the internal light source. This means that we can use standard 1 inch gold plated mirrors with standard mirror mounts as a replacement. The new mirror mounts can be bolted to the breadboard of the spectrometer.

Placing a small mirror in front of the toroidal mirror has the advantage that we do not have to modify any of the original hardware of the Bio-Rad spectrometer. The module with the diaphragm and mirror is also designed to be easily swappable, as this module has to be changed to a different module with only a diaphragm, depending on whether an internal or

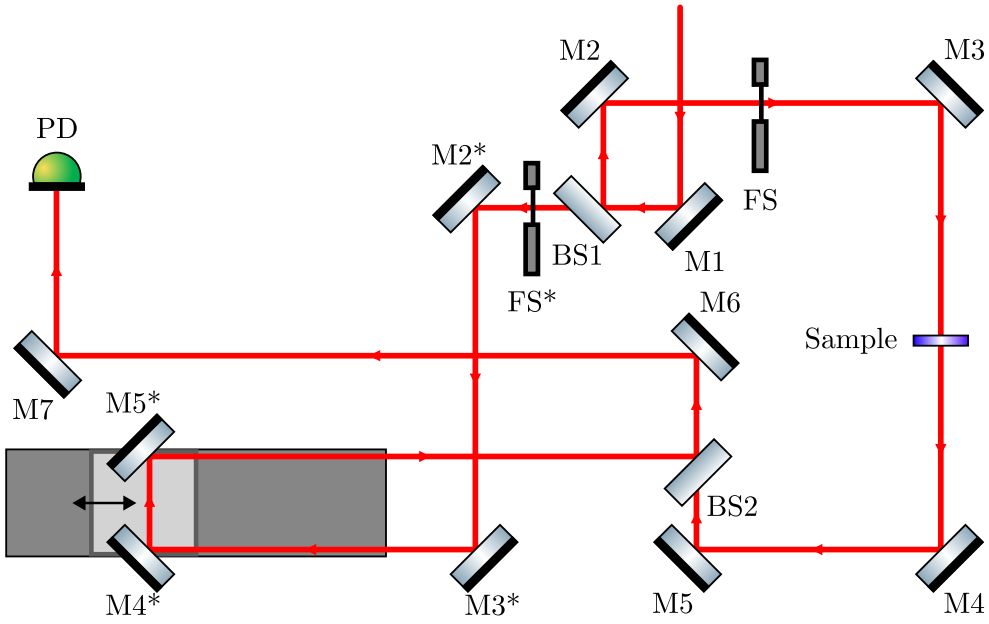

Figure 8: Diagram of the Mach-Zehnder interferometer used for transmission measurements. The light beam enters from the top and is injected into the interferometer via mirror M1. Beamsplitter BS1 splits the light beam into a reference and sample arm. Mirrors M1* to M5* form the reference arm. A linear stage moves M4* and M5* so that the path length can be tuned. Mirrors M1 to M5 form the sample arm. The two interferometer arms are combined by beamsplitter BS2. Finally, mirrors M6 and M7 direct the light onto a photodiode.

external light source is used. This means that all the changes made to the spectrometer are completely reversible and no risk of misalignment of the original hardware is present.

3.2 Transmission Measurement Circuit

Phase sensitive transmission measurements are done using a secondary Mach-Zehnder interferometer, its design is shown in Fig. 8. We use gold plated mirrors and broadband IR plate beamsplitters (BSW23, Thorlabs). The reference arm contains a delay line based on a linear stage so that the path length difference between the reference and sample arm can be fine-tuned. For optimal measurements we want the path length difference between the reference and sample arm to be 400 µm within 200 µm. To accomplish this we first use a fast photodiode to measure the pulse timing difference between the two arms. This allows us to set the path length difference within about 1 cm. After that we can use extra high resolution scans with the Bio-Rad spectrometer to scan a path length difference up to 3 cm, this allows us to measure the path length difference within 1 µm.

For each sample we have to do three measurements, one with both interferometer arms open and two with either arms closed respectively. We are averaging over a large number of scans per measurement to reduce noise, so to minimise artefacts due to slow drifts in the setup

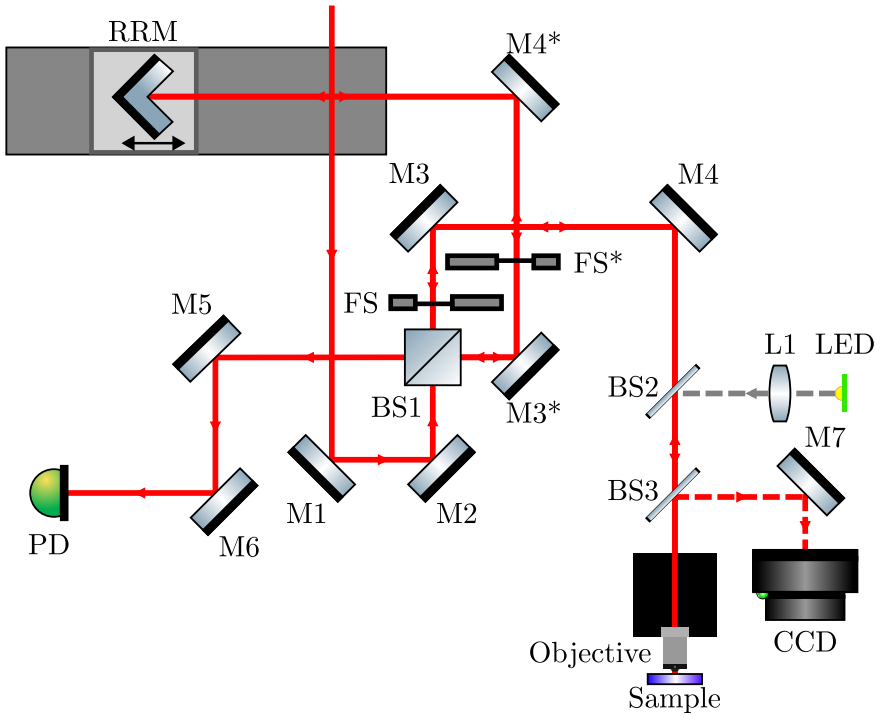

Figure 9: Diagram of the Michelson interferometer used for reflectivity measurements. The light beam enters from the top and is injected into the interferometer via mirrors M1 and M2. Beamsplitter BS1 splits the light beam into a reference and sample arm. Mirrors M3* and M4* and the retro-reflecting mirror RRM form the reference arm. The retro-reflecting mirror is mounted on a linear stage to tune the optical path length. Mirrors M3 and M4 and the objective form the sample arm. Removable beamsplitter BS2 reflects LED light to the sample and removable beamsplitter BS3 reflects light from the sample towards a CCD. This is necessary to aid the alignment of the focus on microscopic samples. Finally, mirrors M5 and M6 direct the light onto a photodiode.

we do the different scans for the three measurements in an alternating fashion. This way we effectively do the three measurements at the same time. We accomplish this by placing a fast shutter (SH05R/M, Thorlabs) in both arms, these shutter can switch within the reset period of the spectrometer. This makes sure that no time is lost waiting on the shutters.

The transmission setup was only used for testing and learning purposes as it was easier to align than the reflectivity setup. No actual measurements were made using this optical circuit.

3.3 Reflection Measurement Circuit

Phase sensitive reflectivity measurements are done using a secondary Michelson interferometer, its design is shown in Fig. 9. We use gold plated mirrors and a broadband IR plate beamsplitter (BSW24, Thorlabs). The path length difference between the sample and ref-

erence arm has to be fine-tuned in the exact same way as the transmission circuit. We also use the same fast shutters for an alternating scanning measurement protocol.

In the sample beam a microscope objective is placed, this allows us to measure reflectivity of microscopic samples. For large samples this is still beneficial, as large samples often suffer from defects. With the objective we can select an area without defects. Due to the broad light spectrum we cannot use ordinary refractive objectives, we use reflective objectives as these do not suffer from chromatic aberrations. There are two mirror objectives available, a x15 NA 0.28 (5001, Beck) objective and a x74 NA 0.65 (5007, Beck) objective. The disadvantage of these objectives is that part of the central area is obstructed. This makes it harder to compare the measurements to theory, as we measure over a somewhat awkward angular distribution.

The reference beam contains a retro reflecting mirror as the microscope objective rotates the beam 180 degrees. The light beam is not completely spatially homogeneous, so for the best overlap of the reference and sample beam we have to give the reference beam the same 180 degrees rotation. A crucial part of alignment is bringing the sample exactly in focus, being of by a few micrometers can mean a decrease in sensitivity of tens of percents. This is due to the sample beam coming back from the objective not having the same level of collimation as the reference beam, causing the overlap of the two beams to decrease rapidly. We optimise the focus by scanning the microscope objective using a piezo-stage (MAX312D/M, Thorlabs) to find the location where the cross-correlate term is maximised.

A LED and a CCD camera are used to aid the alignment of the samples. Pellicle beam-splitters are used to redirect visible LED light to the objective and to redirect light coming back from the objective to the CCD camera. We require pellicle beamsplitters as they have a negligible effect on beam displacement when they are moved in or out of the beam, this way the location of the focus is not affected by the beamsplitters.

3.4 Pulse Detection

The supercontinuum source we use has a pulsed light output with a repetition rate up to 20 kHz and a pulse duration of about 2 ns FWHM. This strongly pulsed nature of the light gives us the means to use a sensitive and low-noise detection scheme. We use an ultra-fast extended InGaAs detector, (Alphalas, UPD-5N-IR2-P) with a spectral range of 800-2600 nm and a rise-time of only 200 ps. This way we can resolve the individual light pulses coming from the light source.

A gated integrator (Stanford Research, SR250) is used to only measure during the duration of each light pulse, with all signals before and after the light pulse being excluded. This leads to a large reduction in background signals and noise. In our case a gate time of 5 ns with a repetition rate of 10 kHz was optimal, meaning that we have a duty-cycle of only 0.005%. The extremely low duty-cycle also shows why lock-in detection is not suitable in our case. There would only be a minimal amount of signal in the lowest order harmonics. Furthermore, lock-in detection would require averaging over many light pulses, making the measurements very slow.

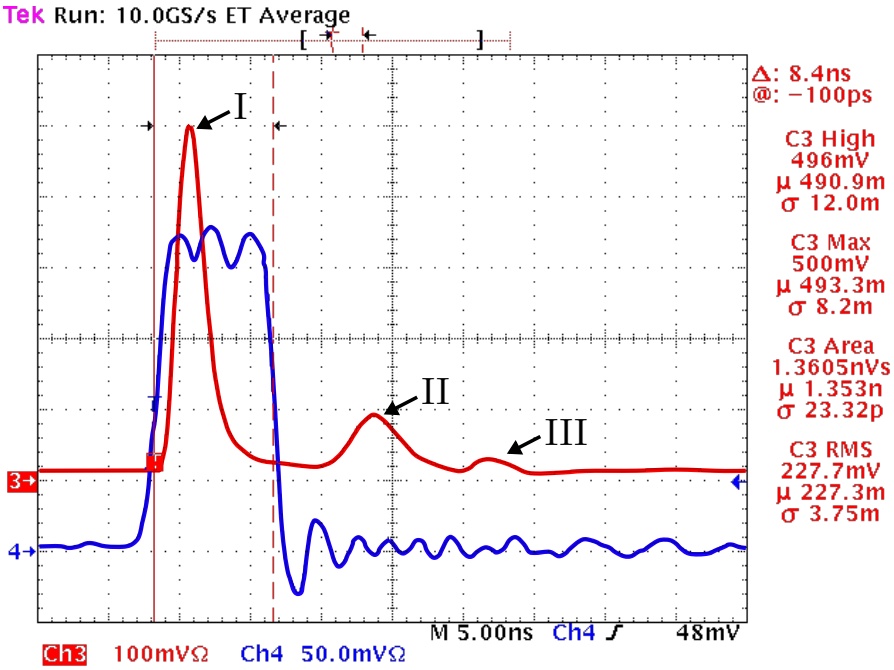

Figure 10: Screenshot of a high-bandwidth oscilloscope. Channel three shows the signal coming from the fast photodiode. We see three pulses, the second and third pulses are generated due to after-pulsing of the seed laser in the super-continuum source. Channel four shows the gating signal of the gated integrator, whenever the gating signal is high the photodiode signal is integrated. The wave-forms are averaged over 500 measurements.

Another way to reduce background signals and noise is by the use of a high-pass filter. We use a 10 kHz high-pass filter between the photodiode and the gated integrator. This gets rid of all $1/f$ noise and slow-varying background signals such as lab lighting. Since the light pulses are so short, more than 99% of the signal power is in frequencies higher than 10 kHz, such that only a minimal amount of signal is lost. The gated integrator is now also used as a DC restoration circuit to bring the signal frequencies back to the measurable domain. To increase sensitivity the high-pass filter can also be replaced with a low-noise RF amplifier. If more sensitivity was needed we used a ZFL-500LN+ amplifier from Mini-Circuits.

To monitor the fast signal we use a high bandwidth oscilloscope (TDS 784D, Tektronix). In Fig. 10 typical wave-forms from the ultra-fast photodiode and gated integrator are shown. This figure shows another advantage of using a gated integrator. The seed laser in the supercontinuum source is a diode pumped Q-switched laser emitting at 1064 nm. This laser suffers from strong after-pulsing, meaning that we get multiple light pulses after our initial pulse. The after-pulses seem random in both timing and power and introduce a significant amount of noise in the measurements. Fortunately there is some separation between the initial light pulse and the after-pulses, so that we can use the gated integrator to temporally filter the after-pulses.

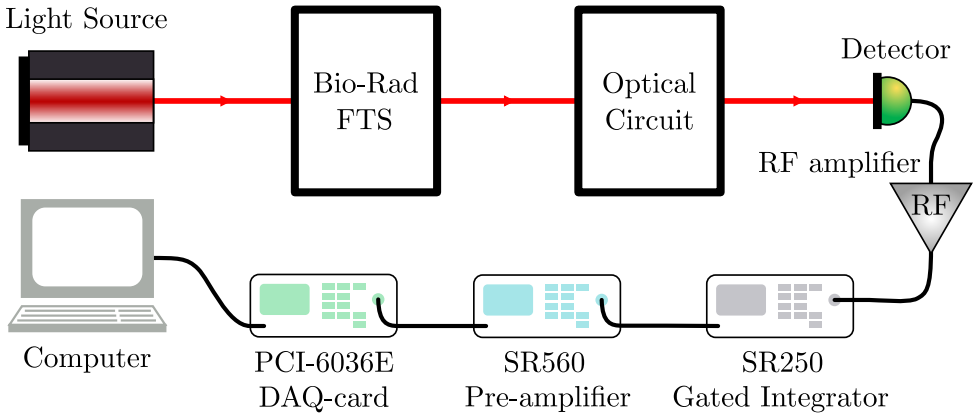

Figure 11: Schematic of the measurement scheme. The supercontinuum source produces short light pulses. These light pulses get modulated by the Bio-Rad Fourier Transform Spectrometer. The modulated light pulses can then be used in any optical circuit desired. After the optical circuit the light pulses get measured by an ultra-fast detector and converted to electrical pulses. A RF amplifier amplifies the electrical pulses to increase the detection sensitivity. Instead of a RF amplifier a band-pass filter can also be used if the increased sensitivity is not necessary. A gated integrator measures only during the pulses and as such both reduces noise in the measurements and acts as a dc restoration circuit. The signal then gets further filtered and amplified by a pre-amplifier and then measured by a DAQ-card connected to a computer.

As a final step the output of the gated integrator is filtered and amplified using a low noise voltage pre-amplifier (Stanford Research, SR560). We need a 30 Hz high-pass filter as slow drifts during each scan can lead to artefacts in the results. Furthermore, we need a 10 kHz low-pass filter as an anti-aliasing filter. The final signal is then recorded using a data acquisition card (National Instruments, PCI-6036E). An overview of the measurement scheme is shown in Fig. 11.

Since the light pulses are short, it is very important that we measure at the exact right time, otherwise we would often miss the pulse and only measure noise. To accomplish this we use hardware triggering. The Bio-Rad spectrometer gives a trigger pulse each time a data point is measured. We use this pulse, via a digital delay generator (TGP110, Aim-TTi) to synchronise the supercontinuum source to the spectrometer. The supercontinuum source also produces a trigger pulse each time a light pulse is generated. This pulse is used to precisely time the measurements of the gated integrator. The standard deviation in the delay between the trigger pulse and the arrival of the light pulse is only 140 ps, which is good enough in our case.

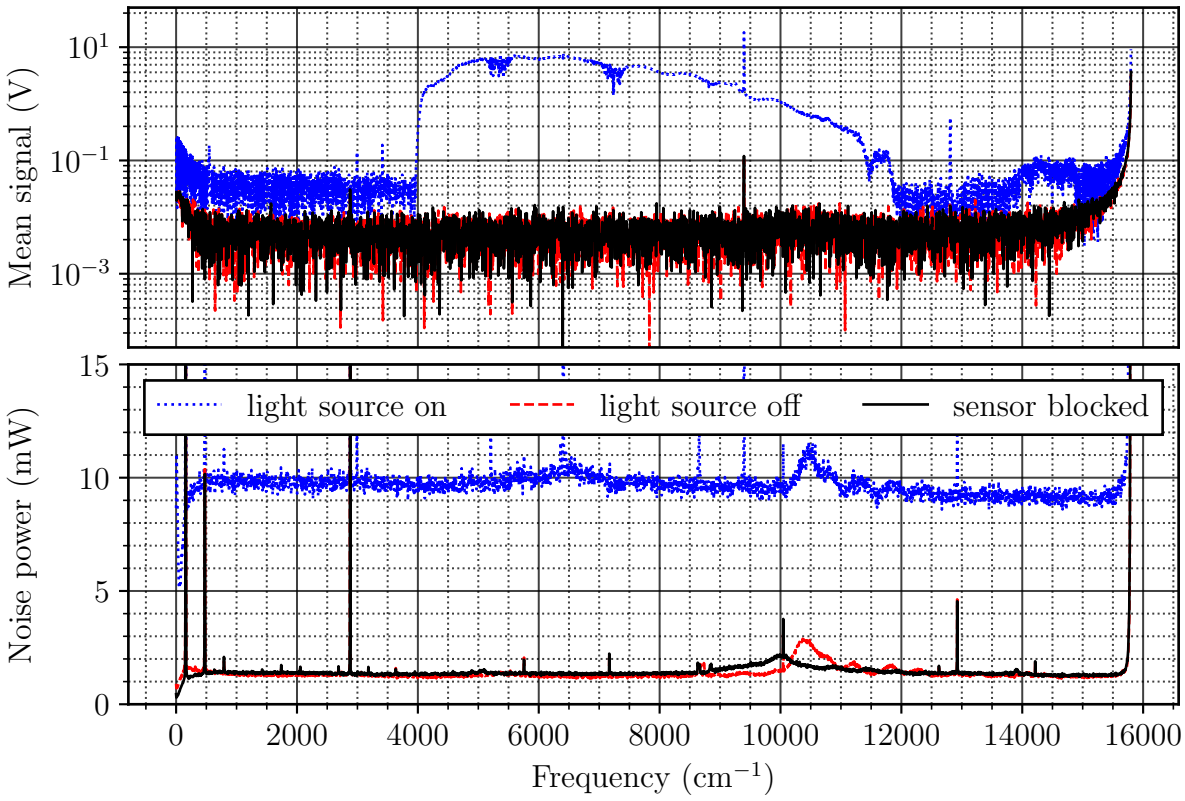

Figure 12: To understand the noise sources we measured the average signal and the noise power for three cases. First, we measure with the detector blocked so that no light can reach the photodiode, this is a measure of the total noise generated by the measurement devices. Secondly, we measure with the detector unblocked and the light source off so that ambient light can be detected. There is barely any difference between the two measurements, which shows the effectiveness of the background rejection with gated integration. Thirdly, we measure with the detector unblocked and the light source on. We find that the noise power in the light itself makes up about 85% of the total noise power, probably due to random intensity noise. A total of 2000 scans were taken per measurement.

3.4.1 Noise Analysis

We went through great lengths in trying to reduce the noise in our measurements. Therefore we study the noise characteristics of three different measurements to determine the effectiveness of our efforts. First, we do a measurement with the detector blocked so that no light can reach the photodiode. This way we measure the noise intrinsic to the used measurement devices. A lower noise level than this cannot be reached without changing the used measurement devices. Secondly, we do a measurement with the detector unblocked, but with the light source off. We then measure both the noise from the measurement devices and noise from background light. Thirdly, we do a measurement with the detector unblocked and with

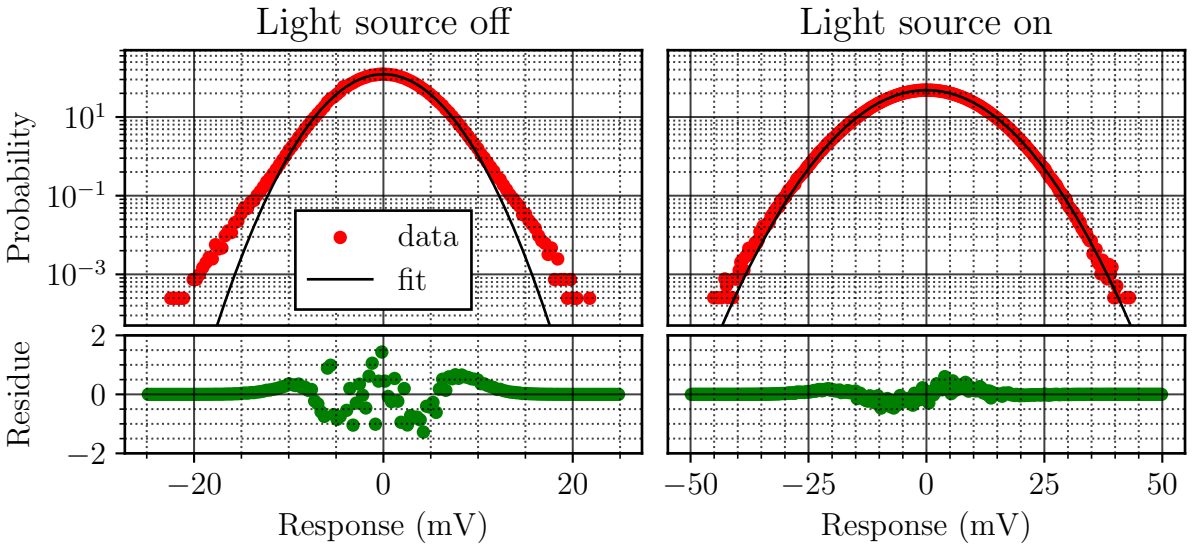

Figure 13: Gaussian fit of the probability distributions of the measured responses with either the light source off or on. In both cases we find that the probability distributions are close to normal distributions, with the exception of the wings. With the light source off we find a standard deviation of 3.24 mV and with the light source on we find a standard deviation of 8.25 mV.

the light source on. This gives us the total noise in our measurements.

The results of the three measurements are shown in Fig. 12, we used 2000 scans for each measurements. It should be noted that we left lab lighting on, so that plenty of background light is present. We find that the measured noise power in all three cases is reasonably flat, which is typical for white noise, except for a number of sharp peaks. The sharp peaks are likely electronic noise due to clock signals of nearby devices. In all cases we find that the peaks disappear when we average over a large number of scans, showing that the phase of these peaked signals are not correlated to the sample-rate of the scans. The mean signals background levels have the same order of magnitude that we would expect if we were to assume Gaussian statistics with the measured noise powers, this again indicates white noise.

An interesting feature is the sharp peak at the rightmost side of the spectrum. We suspect that this is caused by jitter of the trigger signal coming from the light source. Depending on the repetition rate of the light source this jitter can be up to a microsecond, which is very noticeable. Fortunately the peak is far enough out of the region of interest, so that this does not cause any problems.

The measurement with the light source off only has an average of 5% more noise power than the measurement with the detector blocked, this shows the effectiveness of the background suppression of our pulse detection scheme. By comparing the measurement with the light source on to the measurement with the light source off we find that about 85% of the total noise power is present in the supercontinuum light. A large part of this noise is suspected

to come from random intensity noise, supercontinuum sources are known to have relatively large intensity fluctuations per pulse. From this we conclude that there is no sense in further reducing noise in the measurement scheme. The noise present in the light itself, which to our knowledge cannot be filtered out, is much larger than other noise contributions, so that a reduction of noise from other sources will have a negligible effect on the total measurement noise.

To verify whether the noise characteristics are truly Gaussian we have to look at the probability distribution of the measured photodiode responses. This is shown in Fig.13 for the measurements with the light source off and on respectively. In both cases we find that the probability distributions are close to a normal distribution, except for the wings which seem to have a somewhat exponential decay. With the light source off we have a standard deviation of 3.24 mV and with the light source on we have a standard deviation of 8.25 mV. Here we again find that about 85% of the noise power is present in the light itself.

3.4.2 Sensitivity

To get an indication of the sensitivity of our pulse measurement scheme we decided to compare the light intensity measured with a broadband optical power detector to the voltage generated by our photodiode. We also measure the light intensity at different positions in our setup. This shows us possible bottlenecks in the experimental setup, where a lot of light is lost. The optical power is measured using a handheld power meter console (PM400, Thorlabs) and a thermopile sensor (S405C, Thorlabs). The sensor has a reasonably flat response over the entire spectral range of our light source with less than 4 percent variations. It should be noted that the spectral response of the photodiode is only reasonably flat in a spectral range of 1.9 µm to 2.4 µm. Outside this range the sensitivity decreases rapidly. Furthermore, the error of the power sensor is generally much less than the magnitude of the slow variations in light power, so we do not bother doing an error analysis here.

The supercontinuum light source generates 38.9 mW at a repetition rate of 10 kHz. Interestingly, this is significantly less than the manufacturer advertises, we would expect at least 55 mW at this a repetition rate. Of this light only 8.4 mW is left after the Bio-Rad spectrometer. We suspect that most of this light is lost in the beamsplitter of the spectrometer, as a lot of parasitic reflection are visible. The light then goes through a variable ND filter and a beam expander, after this 2.1 mW is left. A lot of light is lost here due to the beam expander having a too large magnification, a large part of the expanded beam is clipped by the output aperture. If in the future more light is needed, a 1.5x beam expander with adjustable focus would be an option. Finally, we have a quarter-wave plate and a polarizer, after this we are left with about half a milliwatt to use in the optical circuit. Due to the low light intensity we could not accurately measure the light power further in the optical circuit.

To determine the sensitivity of the photodiode we measured the light directly after the beam-expander. With the thermopile power detector we measured an optical power of 2.3 mW. We then used a parabolic mirror to focus the beam onto the photodiode. To not completely overwhelm the photodiode we had to place a ND4 filter before the detector, this filter has about 0.1 % transmission in the near infra-red. Using our high bandwidth oscilloscope we

measured $370 \pm 15\,\mathrm{mV}$ peak pulses coming from the detector. From experience we know that about 700 mV peak is the maximum signal before we start to get issues with saturation of the detector. This means that about $4\,\mu\mathrm{W}$ of average incident power onto the detector is optimal. With more light we saturate the detector and with less light we have a decreased signal to noise ratio.

3.5 Verification of Measurement Accuracy

Even more important than low noise measurements are accurate measurements. A way to verify the accuracy of a measurement device is to measure a simple and well known sample and compare the expected result to the measured result. A simple and well known sample are Bragg stacks, the theoretic complex reflectivity of these samples can be easily calculated exactly using transfer matrix theory. The results of this are shown in section 4.1.

4. Measurements

We measure a wide variety of photonic crystals, these are:

- 1D crystal: Bragg stack with defect.
- 2D crystal: Inverse $\sqrt{2}$ crystal.
- 3D crystals: Woodpile and inverse woodpile.
- Opals: Polystyrene opal and inverse silicon opal.

For each sample we give a short introduction about the crystals' properties and history. We then show the measured complex reflection transfer function by its phase shift and amplitude squared. The amplitude squared is compared to an intensity only reflection measurement. This intensity reflection can be determined from the same measurement data by simply not using the cross-correlate measurement. Ideally, the two reflectivities should be identical, so this can be used as a measure of the reliability of the transfer function measurement, the intensity only measurements are much less sensitive and thus more likely to be correct. Due to limitations of the setup the slope in the measured phase shift has an arbitrary offset, this is due to the path length of the sample arm slightly changing whenever we mount a new sample. However, this should not be a problem, as we are mostly interested in a change of the slope. All our measurements presented in this section have a spectral resolution of about $4.4\,\mathrm{cm}^{-1}$ and are averaged over a thousand scans at a singular spot on the sample.

We were not able to find measurements like ours in literature. The few measurements there are in literature only measure group velocity dispersion, which is done in transmission. The setup we use is very similar to an OCT setup, except we use ultra broadband light and we are interested in a time-delay, not a reconstruction of the internal structure. Knowing the internal structure would of course be very interesting, but we are not able to do this due to the wavelength of the light being too long compared to the structure sizes. The most similar measurement we could find was from Vos et al.[8], where they measured dispersion in and around the L stop-band of an opal using both phase sensitive reflection and transmission measurements. The lack of literature makes it hard to compare our results to the results of others.

We can compare the measured phase by a phase predicted using calculations or simulations. This will be done for the Bragg stack and polystyrene opal crystals, as these are relatively simple to model. For these crystals we will also verify the measured phase by comparing it to phase retrieved from the intensity only measurement using the phase-Intensity Kramers-Kronig relations.[16]

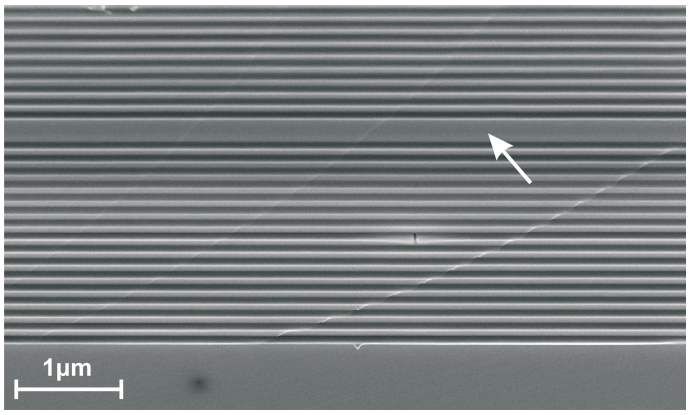

Figure 14: SEM image of a cross section through a similar planar cavity as we studied. The arrow points to the defect layer made of a λ-thick layer of GaAs, above and below are two Bragg mirrors consisting of $\lambda/4$-thick pairs of GaAs (light) and AlAs (dark). Due to the high reflectivity of Bragg mirrors a high Q factor (Q > 1000) can be reached. The structure was made by the group of J.M. Gérard at CEA Grenoble. Image courtesy of A. Hartsuiker.

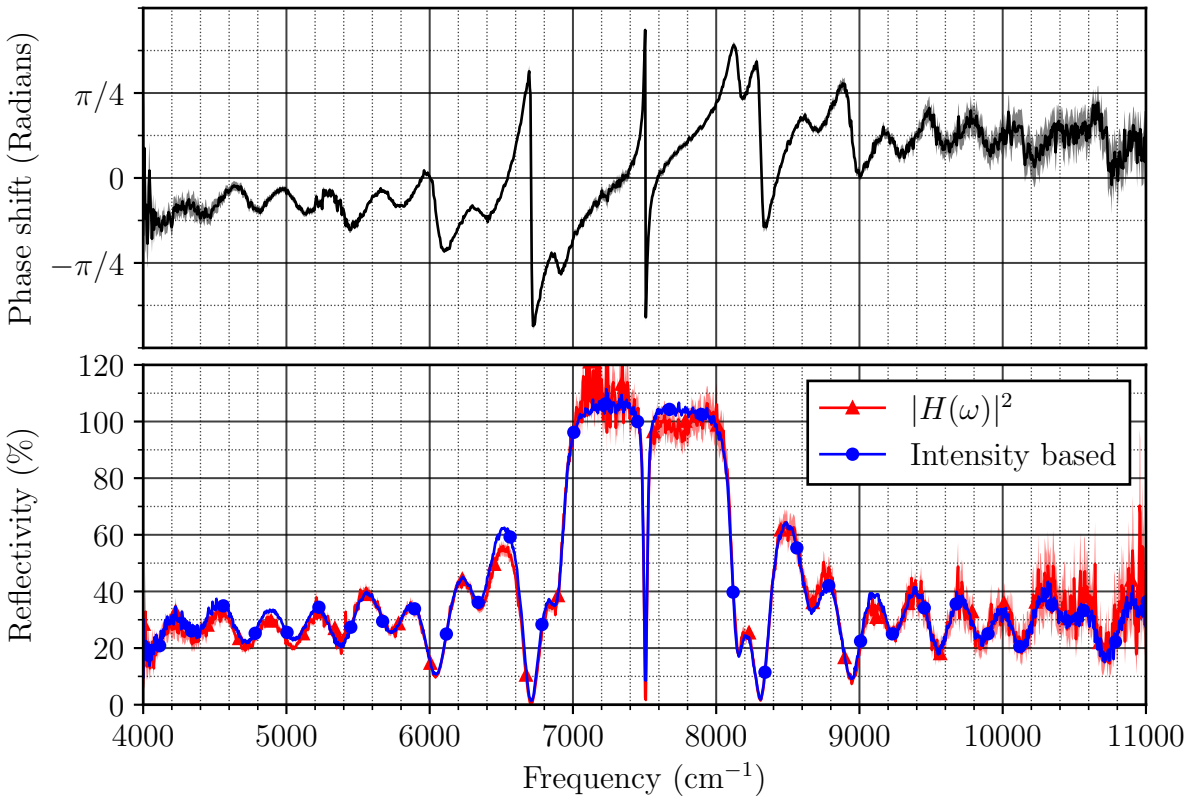

Figure 15: Measured phase shift and squared reflectivity amplitude of Bragg stack cavity AS0059. The red curve is the squared amplitude and the blue curve is the reflected intensity.

4.1 Reflection of a Bragg Stack with defect

One of the candidates for faster and more efficient computers are computers using light opposed to electricity. However, to achieve all optical computing a number of hurdles have to be tackled. For classical computations we needs some way of switching light directly with other light, this is intrinsically a non-linear operation. Ordinarily light only displays non-linear behaviour at extremely high intensities and via interaction with a material. Since efficiency is an important factor for any computation scheme, we have to find some way of switching light without requiring these extremely high intensities. One way of doing this is by using cavities, the cavity acts as an oscillator that temporarily stores the light. This way the interaction strength between materials and light can be increased, as there is simply more time to interact.

The simplest cavities to study are one-dimensional cavities, also known as planar cavities. These cavities generally consist of two mirrors with some space between them. To increase the time that light spends in these cavities we require mirrors with a very high reflectivity. Metallic mirrors are not sufficient, but distributed Bragg reflectors can satisfy the requirements. Such a Bragg stack cavity is shown in Fig. 14, this cavity consists of two $\lambda/4$ Bragg stacks around a central λ-thickness defect layer[17] that breaks the symmetry of the crystal.[18]

We measured cavity *AS0059* which is made with a primary Bragg stack consisting of 8 pairs of 95.5 nm GaAs and 111.6 nm AlAs layers. The cavity layer is made from GaAs and is 382 nm thick and the secondary Bragg stack consist of 12 pairs of 111.6 nm AlAs and 95.5 nm GaAs layers. The cavity was deposited on a {100} GaAs substrate with a 500 nm buffer layer of GaAs in between. The cavity was made by the group of J.M. Gérard at CEA Grenoble and used by Hartsuiker et al.[19] for ultra-fast optical switching of cavities.

Reflection measurements were done with a reflective Schwarzschild objective (15x, NA 0.28). We measured both the complex reflection transfer function as the reflectivity using intensity measurements only. The measured transfer function and the reflectivity are shown in Fig. 15. The magnitude squared of the reflectivity transfer function generally matches the intensity based reflectivity measurements within the standard deviation, this gives us the confidence that the sample was correctly aligned for the measurements. Interestingly, the reflectivity in the stop-band of the Bragg stack appears to be more than a 100%. This is most likely due to our gold reference mirror having a slightly lower reflectivity than expected, perhaps we measured on a slightly contaminated spot on the mirror. The measured phase shift is well defined. At the centre of the cavity resonance ($7506\,\mathrm{cm}^{-1}$) a phase jump appears which is equal to 2.66 ± 0.06 rad within our spectral resolution. This agrees well with a π phase shift within the bandwidth of the cavity resonance.

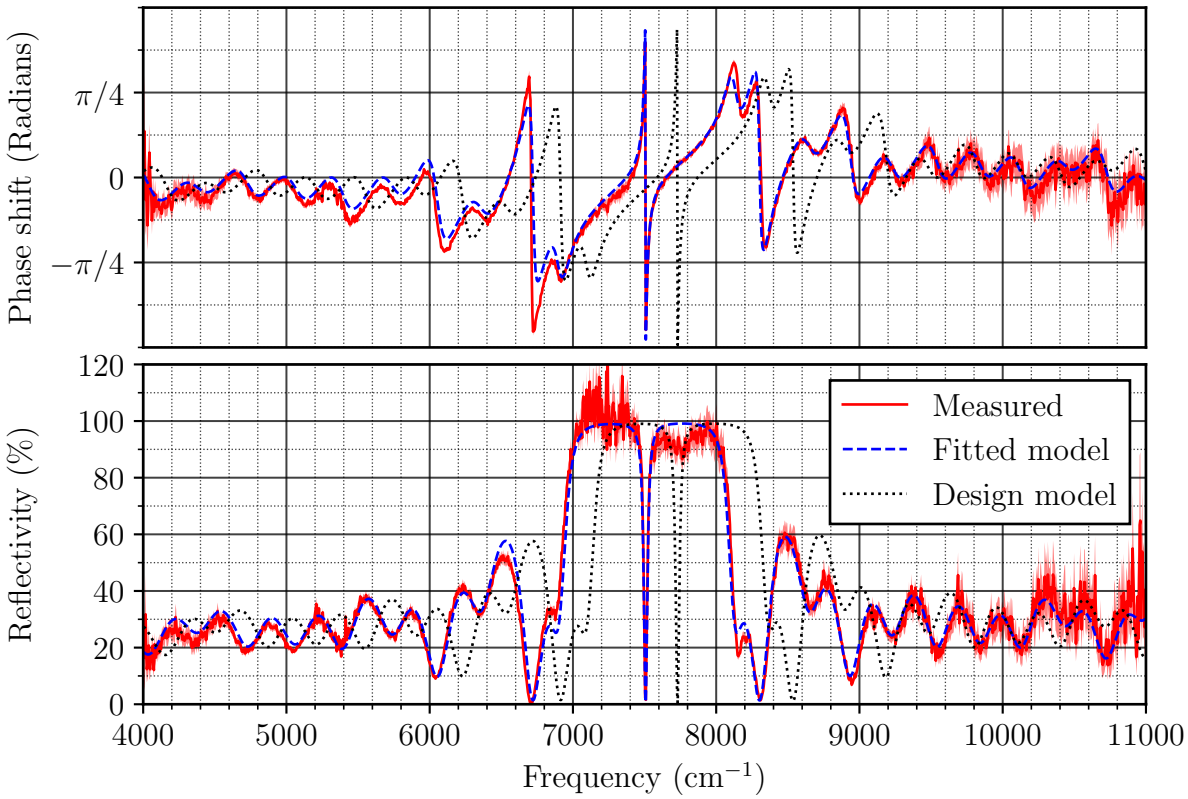

Figure 16: Comparison of the measured reflection transfer function to the transfer function calculated using transfer matrix theory. The black dotted line shows the expected transfer function calculated using the design parameters of the sample. Except for a frequency scaling mismatch the measured and calculated transfer function match well, the scaling mismatch is probably due to the individual layers of the sample being on average slightly thicker than designed. The blue dashed line shows the result of a fit of the reflectivity with a normalisation factor and the thickness of the GaAs and AlAs $\lambda/4$ and GaAs λ layers as free parameters. We see that the fitted model very closely matches both the measured reflectivity and phase shift.

We compare the measured reflectivity transfer function to theory by using the transfer matrix approach, this allows for an exact modelling of the Bragg stack cavity. We took the dispersion of the different materials into account, we used the GaAs and AlAs refractive index from Rakić and Majewski[20] via refractiveindex.info. To compensate for the use of an objective to focus light on the Bragg stack we assume an unpolarized plane wave incident at fourteen degrees normal to the surface of the stack, this is about the average angle of the light exiting the objective. In hindsight this was unnecessary, as the fitting results were the same within error margins whether we compensated for the objective or just took a normal incident plane wave.

The comparison between the measured and modelled reflectivity transfer function is shown in Fig. 16. First we calculate what the expected transfer function is using the design parameters. Except for a frequency scaling mismatch the measured and calculated transfer function match well, the scaling mismatch is probably due to the individual layers of the sample being on average slightly thicker than designed. We then fit the reflectivity with a normalisation factor and the thickness of the GaAs and AlAs $\lambda/4$ and GaAs defect layers as free parameters. The best fit parameters are GaAs $\lambda/4$ layers with a thickness of $98.8 \pm 0.7\,\mathrm{nm}$, AlAs $\lambda/4$ layers with a thickness of $114.3 \pm 0.8\,\mathrm{nm}$ and a defect layer with a thickness of $396.4 \pm 0.8\,\mathrm{nm}$.

We find that the fitted model very closely matches both the measured reflectivity and phase shift. Large differences between the fitted and measured phase only occur where the reflectivity approaches zero, this makes sense as the phase gets less well defined for very small reflectivities. Using the fitted model we also find that the apparent phase jump at the cavity resonance is most likely not a jump, but a very fast, continuous, phase shift. The phase shift is much less than the 2π of an ideal cavity, probably due to a slight mismatch of the cavity to the surrounding Bragg mirrors.

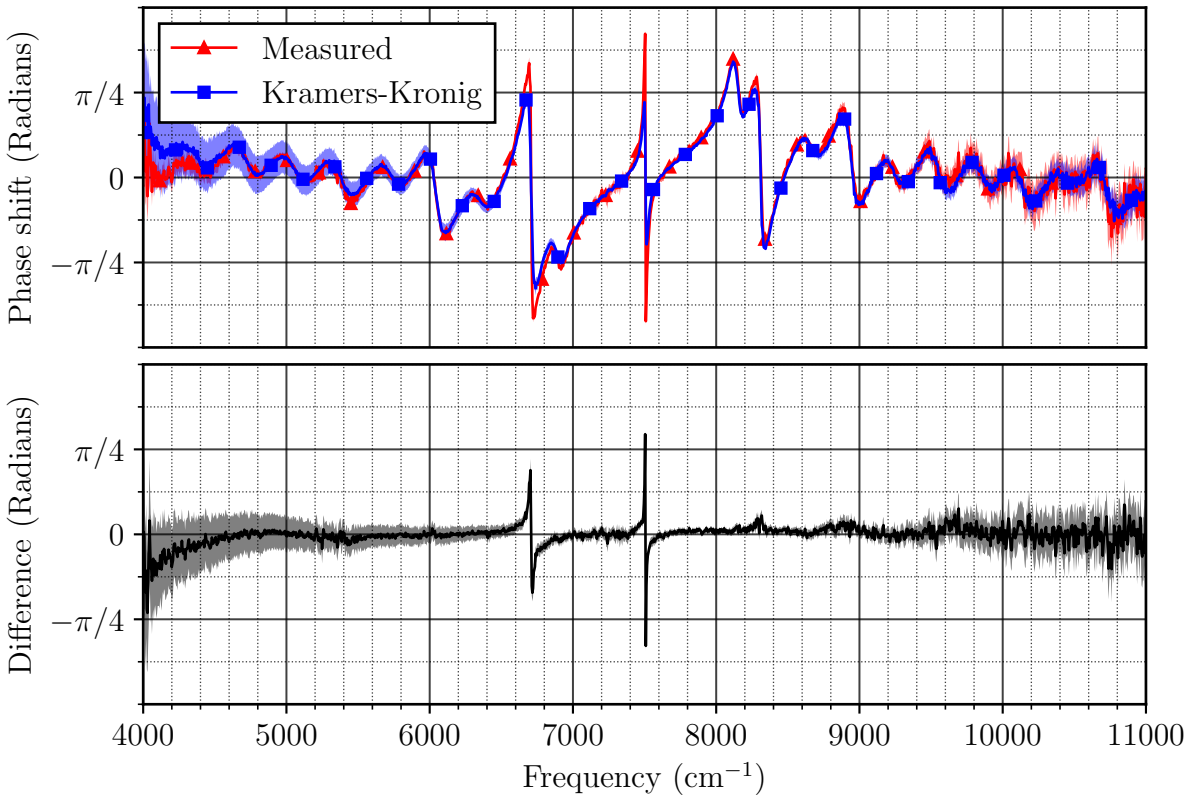

Figure 17: Comparison of the measured phase shift to a phase shift calculated from the intensity only reflectivity, using the intensity-phase Kramers-Kronig relations. The phase shifts generally match within the error margins, with the exception where the measured reflectivity gets very close to zero. This is due to the logarithmic dependence of phase shifts on the intensity, when the reflectivity gets small the phase shift gets more sensitive to small fluctuations in the reflectivity.

As a final step we compare the measured phase shift to a phase shift retrieved from the intensity only reflectivity measurements using the intensity-phase Kramers-Kronig relations,[16] the result of this is shown in Fig. 17. The phase shifts generally match within the error margins, with the exception where the measured reflectivity gets very close to zero. This is due to the logarithmic dependence of phase shifts on the intensity, when the reflectivity gets small the phase shift gets more sensitive to small fluctuations in the reflectivity. The good correspondence between the modelled and measured transfer function and the good correspondence between the measured phase shift and the phase shift retrieved from the intensity-phase Kramer-Kronig relations gives us confidence that the setup yields accurate results.

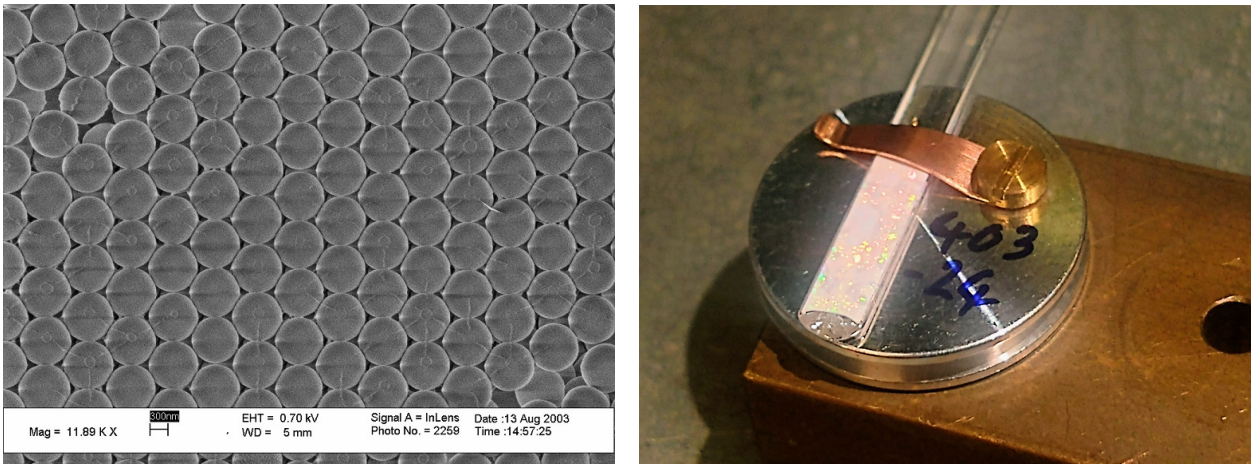

(a) SEM image **(b)** Sample photo

Figure 18: **(a)** SEM image of opal 403-35, it is a similar opal made from the same spheres as the opal we measured. The periodic hexagonal structuring of the first sphere layer is clearly visible. Image courtesy of L. Bechger. **(b)** The measured opal was made by letting suspended polystyrene spheres with a radius of 403 nm slowly settle in a glass cuvette. Many colourful spots show the iridescence from higher order Bragg diffraction.

4.2 Reflection of Opals

4.2.1 Polystyrene Opal

Opals are photonic crystals that consist of periodically stacked dielectric spheres. The opal we will be measuring is fabricated by letting a solution of disperse polystyrene spheres with a radius of 403 nm slowly settle over the course of months. The solvent is evaporated at the same time, so that only air between spheres is left. Under the right circumstances the spheres become close packed and will then often form an FCC crystal structure,[22] an example of the structure is shown in Fig. 18a. The measured opal in its glass cuvette is shown in Fig. 18b.

Reflection measurements were done with a reflective Schwarzschild objective (15x, NA 0.28). Results of the measurements are show in Fig. 19, we see a large reflectivity peak centred at 5400 cm^{-1} with a bandwidth (FWHM) of 460 cm^{-1}. The centre of the reflectivity peak is close to the Bragg condition of the FCC {111} plane.[23] Due to the low refractive index contrast of polystyrene to air this is a stop-band and thus not a complete photonic bandgap.[5] An interesting feature are the fringes, these are especially clearly visible near the stop-gap. We suspect that these fringes are due to defects in the opal as during the drying phase of opal fabrication micro-cracks tend to appear.

The measured phase shift shows strong group delay dispersion over almost the entire measured spectrum, this is surprising as we would only expect strong group delay dispersion close to the stop-gap. We suspect that the strong group delay dispersion is caused by an artefact in our measurements, this is supported by the large difference in measured reflectivity between the transfer function and intensity based approach. Ideally both methods should

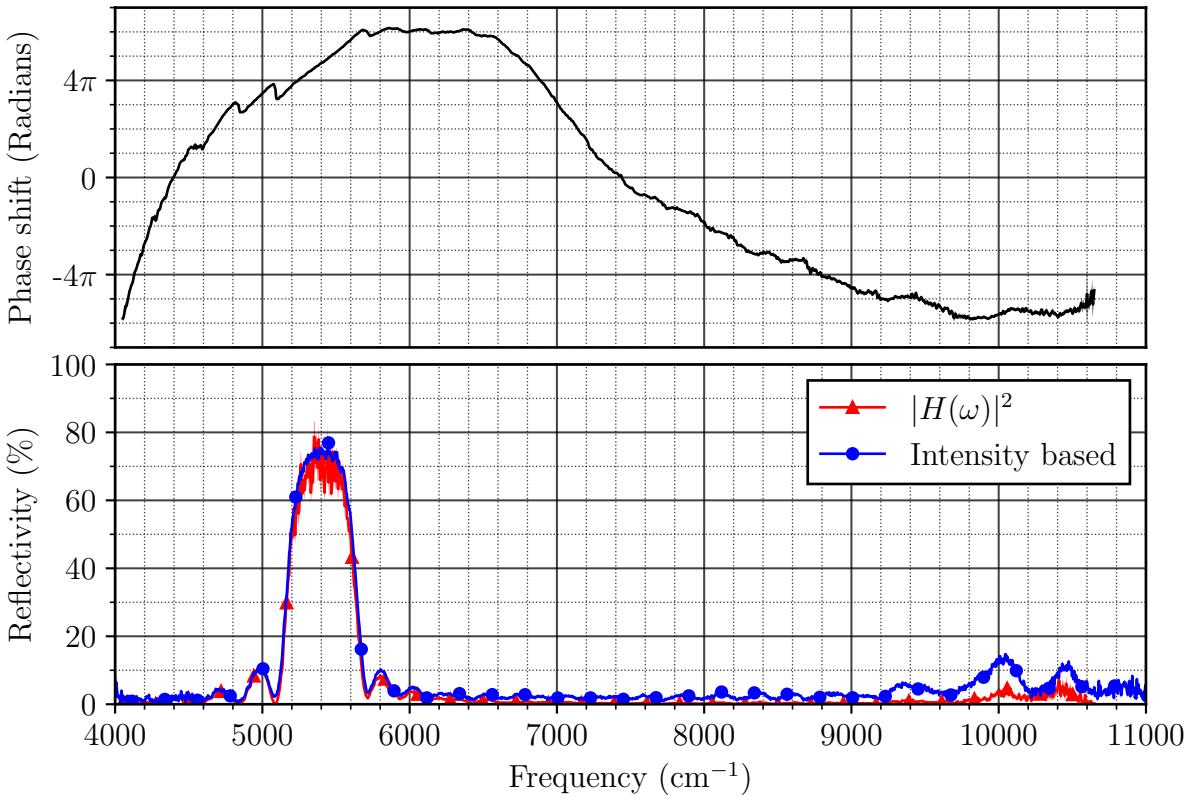

Figure 19: Measured phase shift and squared reflectivity amplitude of opal 403-24. The red curve is the squared amplitude and the blue curve is the reflected intensity.

yield the same reflectivity, but we find that beyond 6000 cm^{-1} the differences in reflectivity can be more than a factor ten apart.

We optimise the focus on samples by maximising the overlap between the sample and reference beam. The opal mainly reflects light in the narrow stop-band, while the gold reference mirror reflected all light almost equally. We know that the collimation of the supercontinuum light changes slightly as function of wavelength, meaning that the maximum overlap for the opal sample yields a different focus distance than for the gold mirror. This causes a sample dependent change in sensitivity response we cannot compensate for that could explain the large reflectivity difference between the transfer function and intensity based methods. The large apparent group delay dispersion is then an artefact caused by the changing sensitivity.

To better understand the measurement results we model the reflectivity of an ideal, infinitely thick opal. A simple model that still captures a lot of the characteristics of opals is the stratified effective index model.[21] This is a one-dimensional transfer matrix model where we divide the opal in a large number of thin slabs. The refractive index for each slab is calculated by taking the average dielectric constant, depending on the fraction of the slab that is filled with polystyrene or air. The model starts in air, then we have a transition

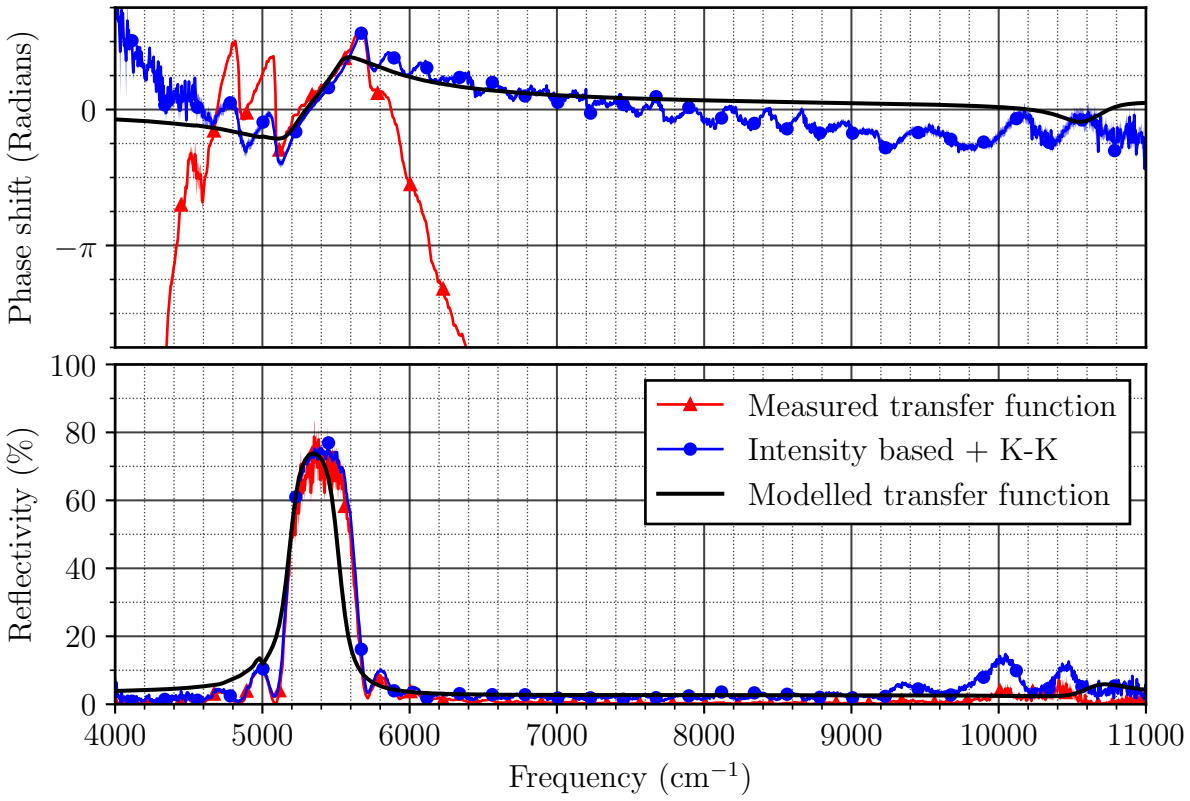

Figure 20: Resulting transfer function calculated from the stratified refractive index model to the measured transfer function.[21] We compare the calculated transfer function to the measured transfer function and to a transfer function retrieved from the intensity based reflectivity, where the phase shift is calculated from the intensity-phase Kramers-Kronig relations.[16]

region from air to opal with the width of a sphere radius, here the filling fraction of the slabs increase quadratically with distance. After that we have endlessly repeating unit cells, for the filling fraction of the unit cell slabs we decided to use a FCC unit cell where we move along the {111} direction. From our previous findings we know that this is most likely to be close to the actual measurement situation.

In any real opal some light is lost due to scattering, to model this we added an additional imaginary term to the refractive index that linearly increases with frequency. We choose for a linear increase as shorter wavelength light more efficiently scatters on defects than long wavelength light, the coefficient was chosen such that the peak reflectivity of the model matches our measurements. Since we do not know the orientation of the opal with respect to the used polarisation, we assume unpolarised light for generality. For the refractive index of polystyrene we used data from Zhang et al.[24,25] via refractiveindex.info. Furthermore, to model the effect of the used microscope objective we average over the angular distribution of light coming from the objective.

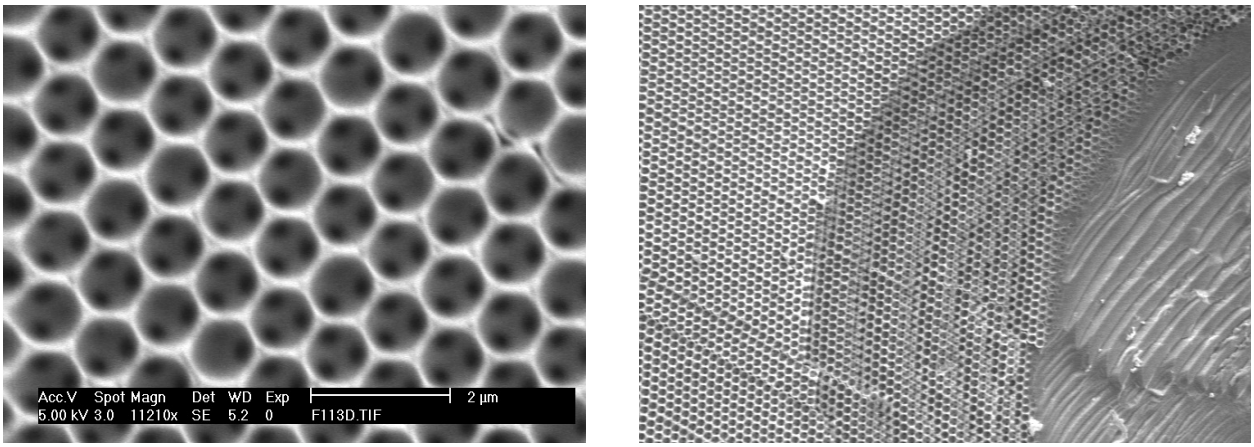

(a) Detail image **(b)** Terracing at the edge

Figure 21: **(a)** SEM image of the inverse opal structure, from this the lattice constant was determined to be $a = 1427 \pm 20\,\text{nm}$.[26] The three black dots in each air sphere are openings to the neighbouring air spheres. **(b)** This SEM image shows terracing of the individual layers the inverse opal is made from. The terracing was made by removing smaller and smaller parts of each layer until the silicon substrate was reached. We can count that the opal consists of seven layers with what appears to be a FCC lattice structure. Both pictures courtesy of J. Kalkman

The results from the model, shown in Fig. 20, are compared to the measured transfer function and to a transfer function retrieved from the intensity based reflectivity, where the phase shift is calculated from the intensity-phase Kramers-Kronig relations.[16] We find that the lower edge of the stop-band matches very well between the model and measurements, the high edge is further of. The slight difference between model and measurement could be explained if we did not measure exactly parallel to the {111} direction but are of by a few degrees, this is likely the case, but unfortunately we cannot verify that. A difference in the central stop-band frequency of only 1% is still very impressive for such a straightforward model. The slight jump in reflectivity at $5000\,\text{cm}^{-1}$ is most likely caused due to a mismatch between the two data sets, as at $5000\,\text{cm}^{-1}$ we switch from one data set to the other.

The modelled phase shift does not match with the measured transfer function, the modelled phase shift has a relatively flat response while the measured phase shift has massive group delay dispersion. However, the phase shift calculated from the intensity based reflectivity using the intensity-phase Kramers-Kronig relation is very close to the modelled phase shift. This confirms our suspicion that the measured phase shift is not accurate, but has artefacts due to the before mentioned sample dependent sensitivity. In the future it would be advantageous to use a narrow band-pass filter during the focus optimisation process, this way chromatic aberrations can be avoided.

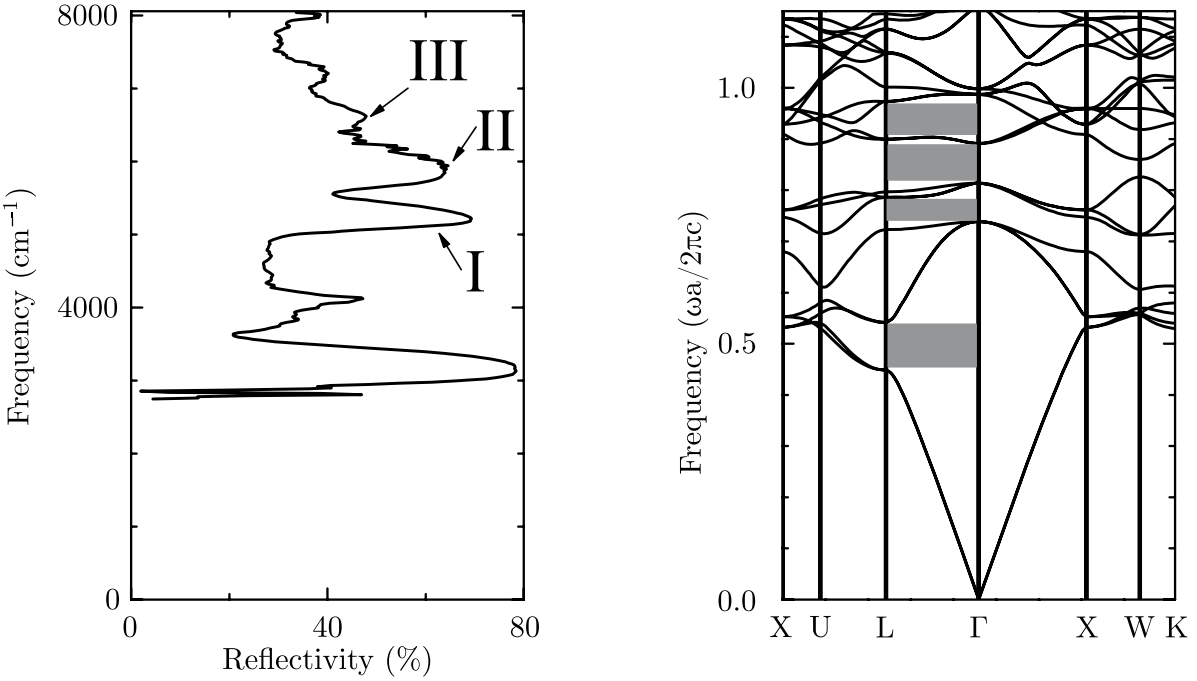

(a) Reflectivity spectrum

(b) Band-structure

Figure 22: **(a)** Reflectivity measurement of the inverse silicon opal by Euser, this is used as a reference for our own measurements. **(b)** Theoretically calculated band-structure of an inverse silicon opal, the y-scale is the same as for the reflectivity spectrum. The band-structure shows that only reflectivity peak II is created a by a complete photonic bandgap, the other reflectivity peaks are created by $\Gamma - \mathrm{L}$ stopbands. Both figures reproduced from the thesis of Euser [27].

4.2.2 Inverse Silicon Opal

An inverse opal is different from a normal opal as it consists of air spheres in a dielectric medium opposed to dielectric spheres in air, meaning that the fraction of dielectric material in the inverse opal is much smaller. The hollow nature of the inverse opal makes it possible to infiltrate the opal with a fluorescent dye, this allows for detection of a modification of the density of states.[28] Inverse opals can have a complete bandgap, given a high enough dielectric contrast.[29]

The type of opal we measure is rather famous, as it is the first reported photonic crystal with bandgap near telecom wavelengths.[30] This particular crystal was made by the Norris group at the University of Minnesota and further processed by Jeroen Kalkman from FOM institute AMOLF in Amsterdam. The crystal was made by first growing a normal opal of silica spheres. Chemical vapour deposition was then used to fill the space between silica spheres with silicon. The silicon was then annealed so that the deposited silicon crystallised into poly-Si. Finally, the silica spheres were etched away, leaving only the silicon shells behind, the result is shown in Fig. 21a. The crystal was used by Euser et al.[26] to demonstrate ultra-fast switching of light with photonic crystals. Since then it has been kept at COPS.

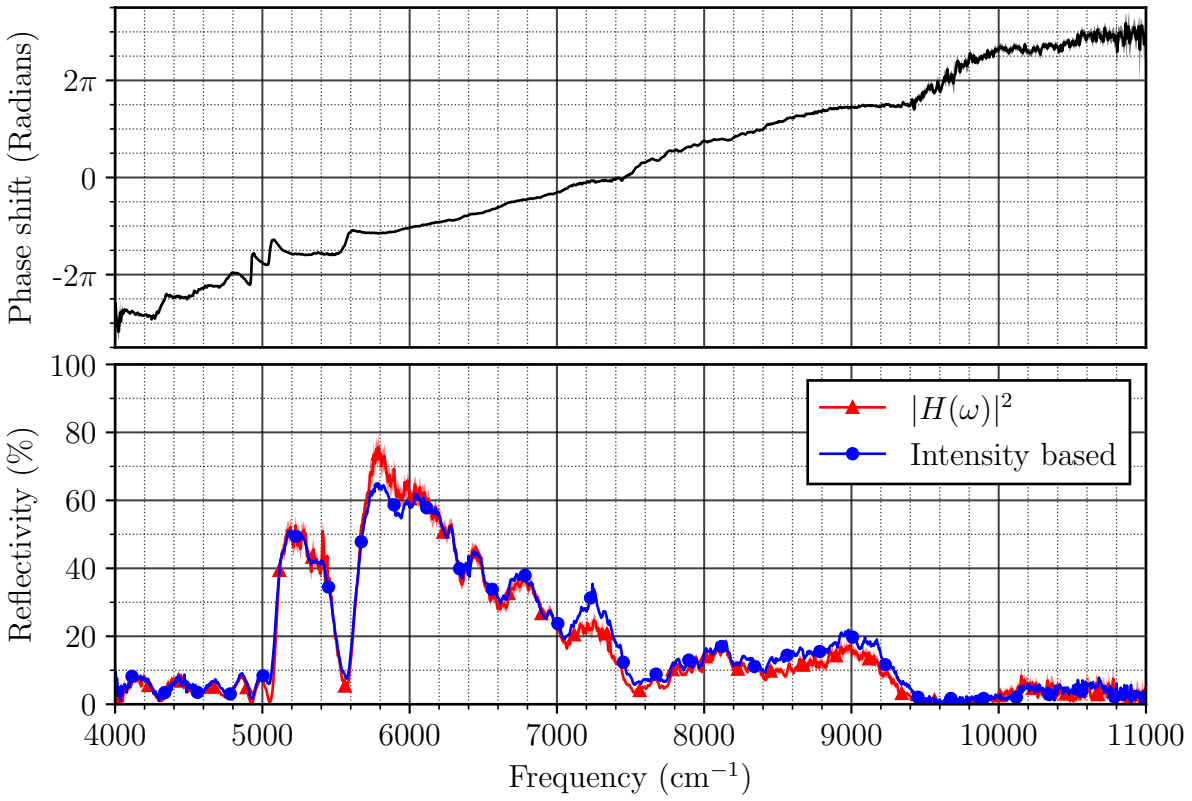

Figure 23: Measured phase shift and squared reflectivity amplitude of inverse opal F113. The red curve is the squared amplitude and the blue curve is the reflected intensity.

From the SEM image shown in Fig. 21b we know that we measure normal to {111} planes of a FCC lattice of the crystal, this corresponds to the $\Gamma - \mathrm{L}$ direction of the band structure. The theoretical band structures in Fig. 22b show that there are four stop-bands in this direction, only the third stop-band is a complete bandgap. Historic measurements from Euser et al. [26] shown in Fig. 22a give a good reference for our own measurements. We see that the four stop-bands correspond to four reflectivity peaks, the first of which we cannot measure, as it is outside our measurement range.

The measurement were done with the same reflective Schwarzschild objective (15x, NA 0.28) as the polystyrene opal, the results are shown in Fig. 23. We find that the reflectivity from the transfer function measurement closely matches the reflectivity from the intensity based measurement, the focus should thus be sufficiently optimised. In the reflectivity spectrum we clearly see reflectivity peak I, but peaks II and III seem to overlap. The phase shift is mostly linear, with the exception of some delay dispersion around reflectivity peak I. This is interesting, as reflectivity peak II is associated with a complete bandgap, but no large phase shift appear next to the peak. This begs the question whether reflection delay measurements are suited for the discrimination of photonic bandgaps.

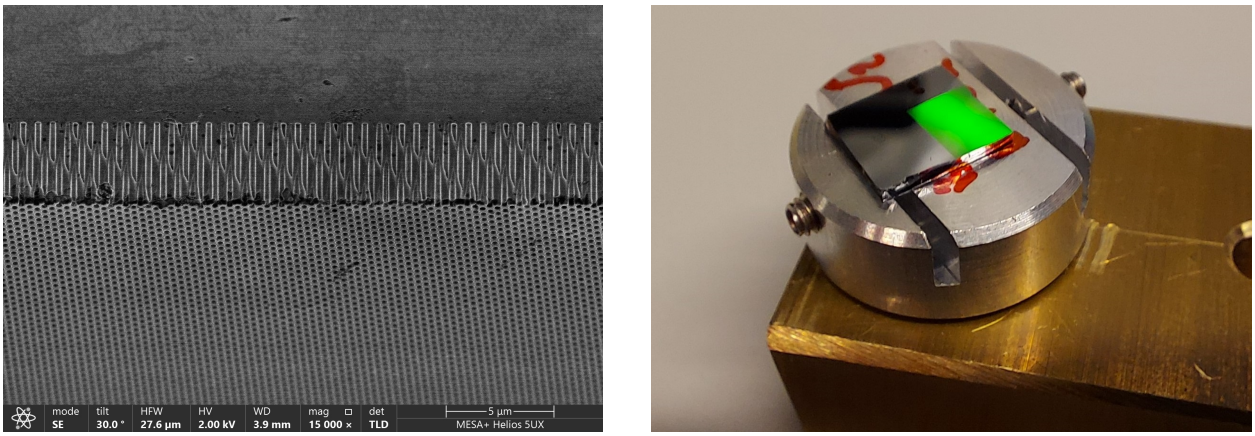

(a) SEM image **(b)** Sample photo

Figure 24: **(a)** SEM image of a cleaved corner of the $\sqrt{2}$ sample. The SEM image shows both the two-dimensional hexagonal pore-structure and the pore-depth. **(b)** The brilliant green hue diffracted from the sample demonstrates the existence of stopbands. Both images courtesy of M. Goodwin.

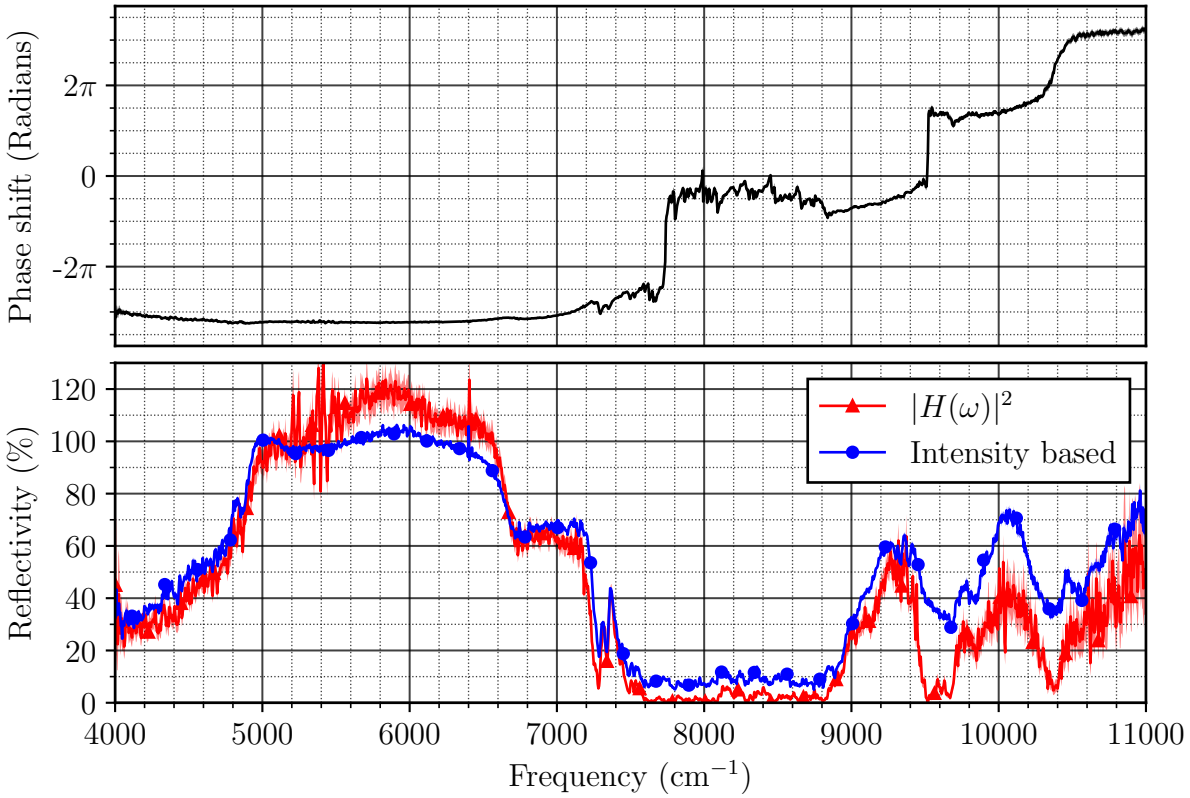

Figure 25: Measured phase shift and squared reflectivity amplitude of $\sqrt{2}$ structure BY01. The red curve is the squared amplitude and the blue curve is the reflected intensity.

4.3 Reflection of Photonic Woodpile crystals

4.3.1 Silicon inverse $\sqrt{2}$ Crystal

A relatively simple type of woodpile crystal is the two-dimensional variant. The crystal consists of air cylinders in silicon, arranged in a centred rectangular lattice. Its name is derived from the ratio of the a and c lattice constants. The structure was made by etching pores in a silicon wafer, the wafer is then cleaved so that we can illuminate the pores from the side. Of course, this is not a real two dimensional crystal, as the cylinders have a very finite length.

The crystal was designed to have a lattice constant a = 688 nm, with a cylinder radius of 122.5 nm. From the SEM image in Fig. 24a we find that the lattice constant is correct within about 1%, but the radius is closer to 135 ± 10 nm. It is hard to find the precise radius, as there is some variation along the length of the pores. We measure from the $\Gamma - \mathrm{M}$ side, with the electric field polarisation perpendicular to the length of the pores. With the given information we can calculate from the Bragg-condition that we would expect a stop-band at $5180\,\mathrm{cm}^{-1}$. However, the higher order stop-band in the visible light range are still very visible, as is shown in Fig. 24b.

Due to the much smaller size of the structure we require a smaller focus spot, we use a reflective Schwarzschild objective with a higher NA to achieve this (74x, NA 0.65). The measurements results are shown in Fig. 25, we find a large stop-band centred at $5900\,\mathrm{cm}^{-1}$ with a large bandwidth (FWHM) of $2700\,\mathrm{cm}^{-1}$. The reflectivity in the stop-band is very high, even appearing to be higher than a 100%, but this is due to the gold reference mirror having a small amount of loss. An interesting feature is the drop in reflectivity at $6600\,\mathrm{cm}^{-1}$, this has not been observed before and it is unclear what the reason for the drop is.

We find that the reflectivity from the transfer function measurement does not match the intensity based reflectivity very well. The reflectivity in the stop-band is somewhat exaggerated, while the reflectivity in the pass-band is largely underestimated. We think that this is not the case due to the focus optimisation problem as with the polystyrene opal. The $\sqrt{2}$ crystal has a very broad reflection band, so that the focus optimisation should give the same results as for a gold mirror. However, in our measurements we have to compensate for small fluctuations in the path length difference of the secondary Michelson interferometer, these are caused by vibrations and air turbulence.

Currently we compensate the path length fluctuations in post-processing by shifting the measured interferograms until the maximum overlap is found. If this is not done correctly it can lead to artefacts in the result, we suspect that this leads to the problems encountered in the measurement. Due to these large reflectivity differences the phase measurement probably has too many artefacts to be accurate, so we cannot make any conclusions about the sample from our phase measurements. In the future it might be advantageous to make the Michelson interferometer actively stabilised with for example the help of a reference HeNe laser. This way the post processing is not necessary anymore so that any problems can be evaded.

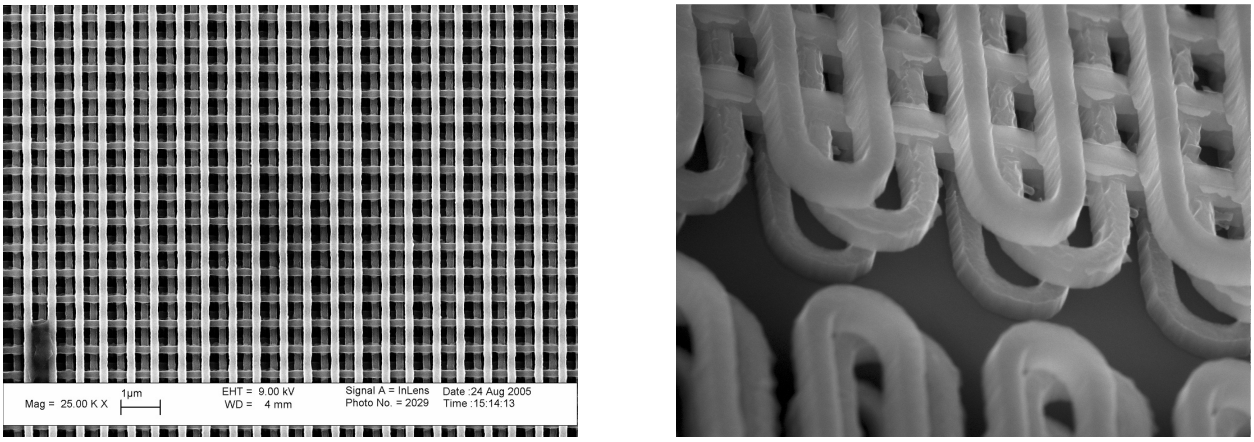

(a) Top view **(b)** Corner Detail

Figure 26: **(a)** SEM image of the top view of crystal C3 from woodpile sample WP1. **(b)** Zooming in on the edge of the crystal shows how the layers are stacked. The entire crystal is made of only five layers of rods, but still has a very wide bandgap with high reflectivity. Both pictures courtesy of T. Euser.

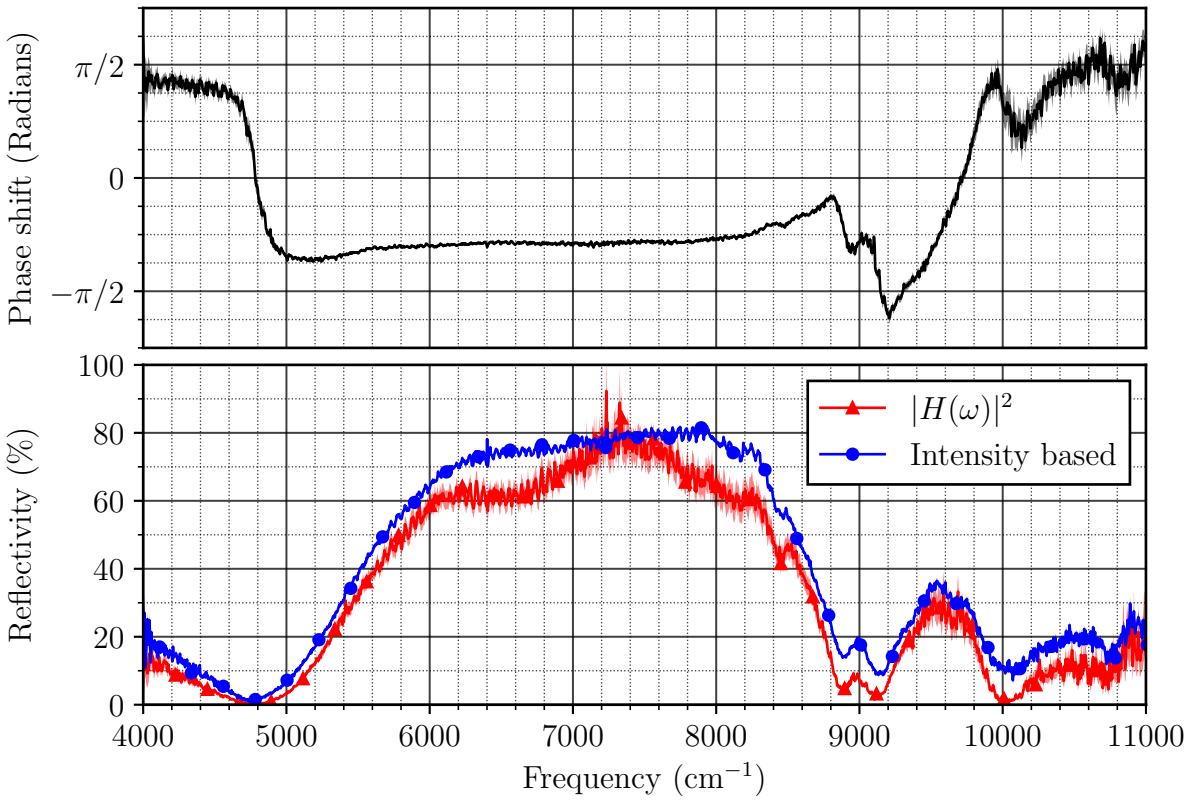

Figure 27: Measured phase shift and squared reflectivity amplitude of woodpile structure WP1, crystal C3. The red curve is the squared amplitude and the blue curve is the reflected intensity.

4.3.2 Silicon Woodpile Crystal

Woodpile crystals have received a lot of attention as they were the first fabricated crystals that exhibited a complete bandgap.[31] Woodpile crystals can have a much wider bandgap than their opal counterparts, while not being too hard to fabricate. We measure woodpile structure WP1, crystal C3. It is part of a larger sample consisting of many crystals, all designed to have a photonic bandgap around telecom wavelengths. Each crystal on the sample has a slightly different geometry, so that there would always be at least one crystal that suited needs. They consist of 5 layers of stacked poly-crystalline silicon nano-rods, this is clearly shown in Fig. 26. The sample was made by Dr. J. Fleming from Sandia and characterised by the Polman group at AMOLF.[32] Euser et al.[33] used the crystals to do ultrafast optical switching.

Measurements are done along the {001} direction of the lattice with a reflective Schwarzschild objective (15x, NA 0.28), the results are shown in Fig. 27. We find a bandgap centred at $7090\,\mathrm{cm}^{-1}$ with a massive bandwidth (FWHM) of $3180\,\mathrm{cm}^{-1}$. The centre of the bandgap contains what appear to be Fabry-Perot fringes with a free spectral range of about $46\,\mathrm{cm}^{-1}$, which corresponds to an optical path length of about $100\,\mu\mathrm{m}$. This is much thicker than the crystal itself, so we suspect that the fringes come from a buffer layer under the crystal. Unfortunately, no details are mentioned about the materials that the crystal is fabricated on, so this cannot be verified.

The reflectivity from the transfer function and from the intensity based approach are relatively close, except that the dips in reflectivity are much more pronounced in the transfer function reflectivity. This appears to be similar to the problems encountered with the $\sqrt{2}$ crystal. Nevertheless, we find that the phase shift is constant in the bandgap and has a significant amount of group delay dispersion at the bandgap edge. Whether the magnitude of the measured phase shifts are accurate is unsure.

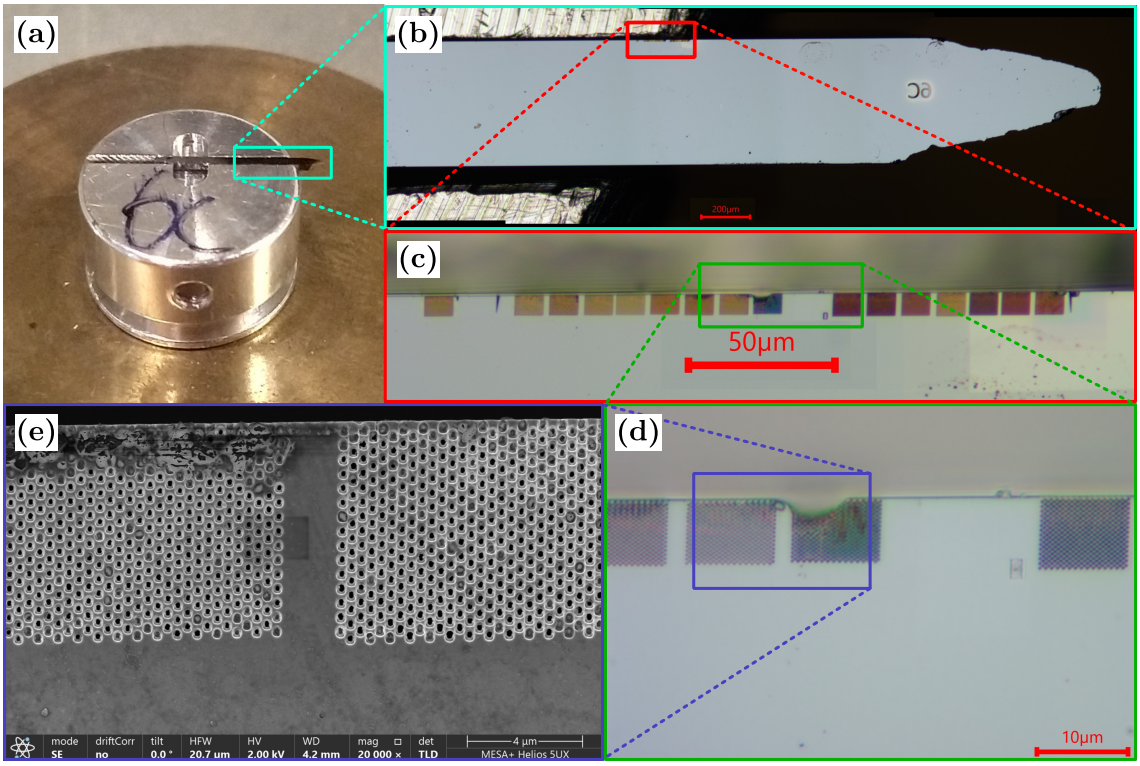

Figure 28: **(a)** Sample holder with silicon bar 6C. **(b)** In the bar a number of crystal structures are etched. **(c)** By zooming further in we can see the structural colours of the different types of crystals. All crystals are designed to have the same lattice constant a = 680 nm, the difference between crystals is the pore radius and whether they have defect pores or not. Visible from right to left are crystals 1 till 16. **(d)** We measure the reflection transfer function of crystal 9, the second crystal visible from the left. Crystal 8 has a large chunk missing, these samples are very delicate and unfortunately sometimes collapse. **(e)** The high resolution of the SEM image allows us to see the entrance shape of the pores. With older samples like this the etching process is not yet optimised as much and the pores often have a somewhat crooked shape. SEM image courtesy of M. Goodwin.

4.3.3 Silicon Inverse Woodpile Crystal

The last crystal we measure is an inverse 3D woodpile crystal, it has a FCC lattice with lattice constant a = 680 nm, c = a/$\sqrt{2}$ and a designed pore radius of 160 nm. From band-structure calculations we would expect a theoretical bandgap starting at 7040 cm^{-1} and ending at 9050 cm^{-1}.[34] An overview of the complete sample is shown in Fig. 28, the SEM image in the overview suggests that the actual pore radius is much smaller than designed. The shape of the pores is also somewhat crooked, due to the etching process not being as optimised yet with older samples like this. The crystal dimensions are about 8 by 10 by 8 µm, due to the small size we require a small focus spot, so we use a high NA reflective Schwarzschild objective (74x, NA 0.65).

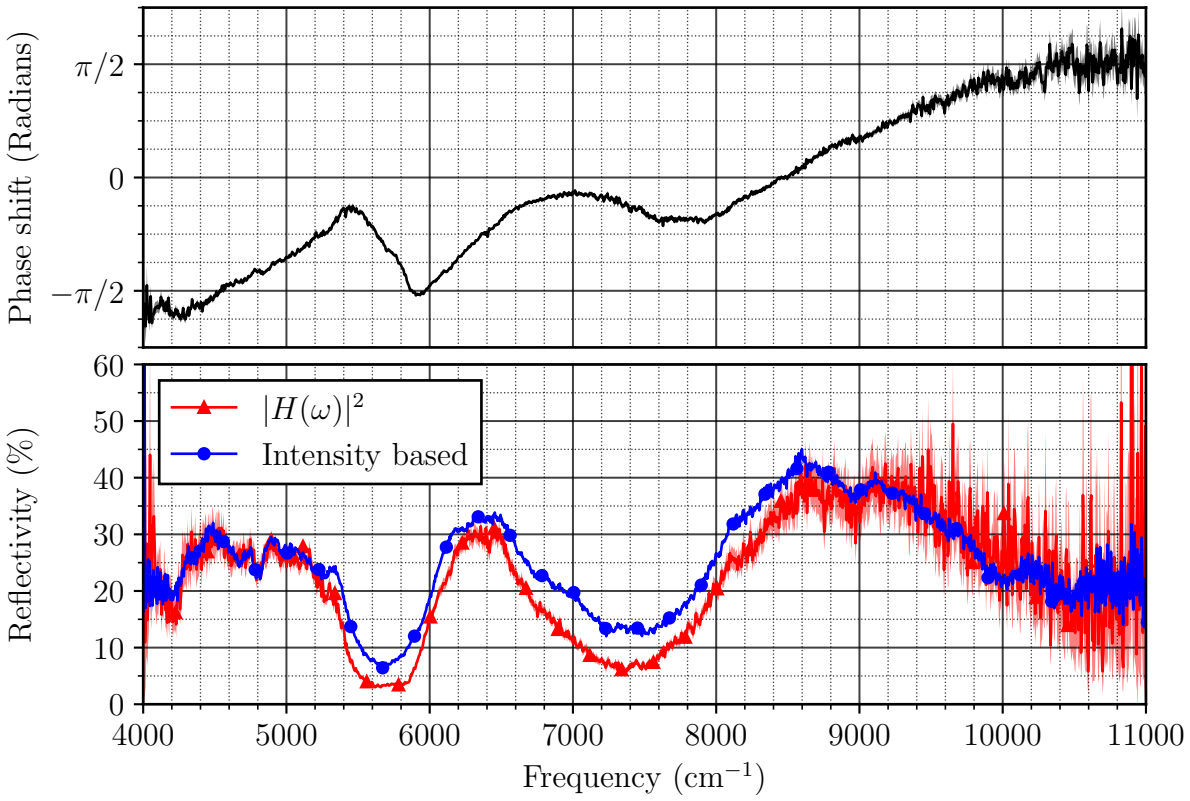

Figure 29: Measured phase shift and squared reflectivity amplitude of inverse woodpile structure bar 6C, crystal 9. The red curve is the squared amplitude and the blue curve is the reflected intensity.

The measurements results are shown in Fig. 29, here we used the silicon of the bar as a reference. We faced the crystal from the side visible in Fig. 28b, with the electric field polarisation parallel to the length of the bar. The peak reflectivities are not as high as with other samples, but we still see significant changes in reflectivity. There is some difference between the reflectivity from the transfer function and the intensity based measurements, we again see that the dips in the reflectivity are more extreme with the transfer function measurements. However, the difference is not so extreme that we cannot use the measured phase shift anymore to make conclusions about the sample.

Around the central reflectivity peak we see a kink in the phase shift at both $5900\,\mathrm{cm}^{-1}$ and $7000\,\mathrm{cm}^{-1}$. This corresponds very well to the theoretical bandgap prediction for a pore radius of 133 nm, this is much smaller than the designed pore radius, which we already expected from the SEM images. In this case the measured phase shift helps significantly to find the bandgap edge, the phase shift has a clear change slope at the edge of the bandgap which serves as a good marker.

5. Conclusion and Discussion

We have build a phase sensitive reflectivity setup based on the method designed by Kop and Sprik[1]. The method was adapted to our needs by placing the Fourier transform spectrometer to the beginning of the optical circuit. For this we had to change some of the spectrometer hardware. Furthermore, we also use a supercontinuum source so that we can measure a large bandwidth starting at 2500 nm to 900 nm. The pulsed nature of the supercontinuum light is used in combination with gated integration to increase the sensitivity and noise performance of the measurements.

We measured a number of photonic crystals. The measurement on the Bragg stack cavity showed that the setup is capable of accurately measuring the phase shift caused by a sample. However, during the measurement of other samples a number of problems became apparent that should be addressed. The first problem is caused by the optimisation of the focus distance. Due to a chromatic aberration in the collimation of the supercontinuum light, the focus optimisation is influenced by the sample we want to measure. This could be solved by using a narrow band-pass filter to minimise the effects of the chromatic aberration.

A second problem in the measurements is caused by path length difference fluctuations in the secondary Michelson interferometer. This could be solved by adding active stabilisation of the interferometer. Even though this would be hard to accomplish, it would be very beneficial to both the measurement results and on the amount of require post-processing.

A third problem with the measurements could have to do with light polarisation. Some amount of the light coming back from the sample is scattered opposed to being reflected. Scattering can change the polarisation state of the light. Two light beams with an opposing polarisation state will not interfere. This means that the light with a different polarisation will not be detected in the transfer function measurement, but it will be detected in the intensity based reflectivity measurements. This might be another reason why the transfer function measurement is often slightly different from the intensity based measurements. The problem can be simple solved by getting a second polarizer and placing it in front of the detector.

In a recent paper Baek and Park[35] showed that it is possible to do holographic imaging using intensity only measurements. This is in agreement with our results for the Bragg stack. In that case the intensity-phase Kramer-Kronig relations could be used to accurately reconstruct the phase shift response from the intensity based measurement. If it turns out that intensity-phase Kramer-Kronig relations can be accurately used to reconstruct the phase shift for all types of samples, then it is unnecessary to do phase sensitive measurements in the first place. Interestingly, that would also mean that current OCT measurement devices are unnecessarily complex. It might therefore be a good idea to investigate this possibility, as intensity only measurements are much simpler.

References

[1] R. H. J. Kop and R. Sprik. Phase-sensitive interferometry with ultrashort optical pulses. *Review of Scientific Instruments*, 66(12):5459–5463, 1995. doi: 10.1063/1.1146069.

[2] J. D. Joannopoulos, P. R. Villeneuve, and S. Fan. Photonic crystals: putting a new twist on light. *Nature*, 386(6621):143–149, March 1997. doi: 10.1038/386143a0.

[3] R. Smaâli, D. Felbacq, and G. Granet. Bloch waves and non-propagating modes in photonic crystals. *Physica E: Low-dimensional Systems and Nanostructures*, 18(4):443–451, June 2003. doi: 10.1016/s1386-9477(03)00183-8.

[4] F. Bloch. Über die quantenmechanik der elektronen in kristallgittern. *Zeitschrift für Physik*, 52(7-8):555–600, July 1929. doi: 10.1007/bf01339455.

[5] P. R. Villeneuve and M. Piché. Photonic bandgaps in periodic dielectric structures. *Progress in Quantum Electronics*, 18(2):153–200, January 1994. doi: 10.1016/0079-6727(94)90007-8.

[6] R. Sprik, B. A. van Tiggelen, and A. Lagendijk. Optical emission in periodic dielectrics. *Europhysics Letters (EPL)*, 35(4):265–270, August 1996. doi: 10.1209/epl/i1996-00564-y.

[7] S. Noda, M. Fujita, and T. Asano. Spontaneous-emission control by photonic crystals and nanocavities. *Nature Photonics*, 1(8):449–458, August 2007. doi: 10.1038/nphoton.2007.141.

[8] W. L. Vos, H. M. Driel, M. Megens, A. F. Koenderink, and A. Imhof. Experimental probes of the optical properties of photonic crystals. In *Photonic Crystals and Light Localization in the 21st Century*, pages 191–218. Springer Netherlands, 2001. doi: 10.1007/978-94-010-0738-2˙15.

[9] K. Naganuma, K. Mogi, and H. Yamada. Group-delay measurement using the fourier transform of an interferometric cross correlation generated by white light. *Optics Letters*, 15(7):393, April 1990. doi: 10.1364/ol.15.000393.

[10] S. Diddams and J.-C. Diels. Dispersion measurements with white-light interferometry. *Journal of the Optical Society of America B*, 13(6):1120, June 1996. doi: 10.1364/josab.13.001120.

[11] I. Zorin, J. Kilgus, K. Duswald, B. Lendl, B. Heise, and M. Brandstetter. Sensitivity-enhanced Fourier transform mid-infrared spectroscopy using a supercontinuum laser source. *Applied Spectroscopy*, 74(4):485–493, feb 2020. doi: 10.1177/0003702819893364.

[12] R. de Laer Kronig. On the theory of dispersion of x-rays. *Journal of the Optical Society of America*, 12(6):547, jun 1926. doi: 10.1364/josa.12.000547.

[13] H. A. Kramers. La diffusion de la lumière par les atomes. In *Atti Cong. Intern. Fisica (Transactions of Volta Centenary Congress) Como*, volume 2, pages 545–557, 1927.

[14] B. Y.-K. Hu. Kramers–kronig in two lines. *American Journal of Physics*, 57(9):821–821, sep 1989. doi: 10.1119/1.15901.

[15] J. Tellinghuisen. Statistical error propagation. *The Journal of Physical Chemistry A*, 105(15):3917–3921, March 2001. doi: 10.1021/jp003484u.

[16] R. H. Kop, P. de Vries, R. Sprik, and A. Lagendijk. Kramers-Kronig relations for an interferometer. *Optics Communications*, 138(1-3):118–126, May 1997. doi: 10.1016/s0030-4018(97)00061-8.

[17] J. M. Gérard, D. Barrier, J. Y. Marzin, R. Kuszelewicz, L. Manin, E. Costard, V. Thierry-Mieg, and T. Rivera. Quantum boxes as active probes for photonic microstructures: The pillar microcavity case. *Applied Physics Letters*, 69(4):449–451, July 1996. doi: 10.1063/1.118135.

[18] J. D. Joannopoulos, S. G. Johnson, J. N. Winn, and R. D. Meade. *Photonic Crystals - Molding the Flow of Light*. Princeton University Press, March 2008. ISBN 9780691124568.

[19] A. Hartsuiker, P. J. Harding, Y.-R. Nowicki-Bringuier, J.-M. Gérard, and W. L. Vos. Kerr and free carrier ultrafast all-optical switching of GaAs/AlAs nanostructures near the three photon edge of GaAs. *Journal of Applied Physics*, 104(8), October 2008. doi: 10.1063/1.3000098.

[20] A. D. Rakić and M. L. Majewski. Modeling the optical dielectric function of GaAs and AlAs: Extension of adachi's model. *Journal of Applied Physics*, 80(10):5909–5914, November 1996. doi: 10.1063/1.363586.

[21] I. Maurin, E. Moufarej, A. Laliotis, and D. Bloch. Optics of an opal modeled with a stratified effective index and the effect of the interface. *Journal of the Optical Society of America B*, 32(8):1761, July 2015. doi: 10.1364/josab.32.001761.

[22] D. Gasperino, L. Meng, D. J. Norris, and J. J. Derby. The role of fluid flow and convective steering during the assembly of colloidal crystals. *Journal of Crystal Growth*, 310(1):131–139, January 2008. doi: 10.1016/j.jcrysgro.2007.09.034.

[23] S. G. Romanov, T. Maka, C. M. S. Torres, M. Müller, R. Zentel, D. Cassagne, J. Manzanares-Martinez, and C. Jouanin. Diffraction of light from thin-film polymethylmethacrylate opaline photonic crystals. *Physical Review E*, 63(5), April 2001. doi: 10.1103/physreve.63.056603.

[24] X. Zhang, J. Qiu, X. Li, J. Zhao, and L. Liu. Complex refractive indices measurements of polymers in visible and near-infrared bands. *Applied Optics*, 59(8):2337, March 2020. doi: 10.1364/ao.383831.

[25] X. Zhang, J. Qiu, J. Zhao, X. Li, and L. Liu. Complex refractive indices measurements of polymers in infrared bands. *Journal of Quantitative Spectroscopy and Radiative Transfer*, 252:107063, September 2020. doi: 10.1016/j.jqsrt.2020.107063.

[26] T. G. Euser, H. Wei, J. Kalkman, Y. Jun, A. Polman, D. J. Norris, and W. L. Vos. Ul-

trafast optical switching of three-dimensional si inverse opal photonic band gap crystals. *Journal of Applied Physics*, 102(5):053111, September 2007. doi: 10.1063/1.2777134.

[27] T. Euser. *Ultrafast Optical Switching of Photonic Crystals*. PhD thesis, University of Twente, mar 2007.

[28] H. P. Schriemer, H. M. van Driel, A. F. Koenderink, and W. L. Vos. Modified spontaneous emission spectra of laser dye in inverse opal photonic crystals. *Physical Review A*, 63(1), December 2000. doi: 10.1103/physreva.63.011801.

[29] H. S. Sözüer, J. W. Haus, and R. Inguva. Photonic bands: Convergence problems with the plane-wave method. *Physical Review B*, 45(24):13962–13972, June 1992. doi: 10.1103/physrevb.45.13962.

[30] A. Blanco, E. Chomski, S. Grabtchak, M. Ibisate, S. John, S. W. Leonard, C. Lopez, F. Meseguer, H. Miguez, J. P. Mondia, G. A. Ozin, O. Toader, and H. M. van Driel. Large-scale synthesis of a silicon photonic crystal with a complete three-dimensional bandgap near 1.5 micrometres. *Nature*, 405(6785):1476–4687, jun 2000. doi: 10.1038/35013024.

[31] S. Y. Lin, J. G. Fleming, D. L. Hetherington, B. K. Smith, R. Biswas, K. M. Ho, M. M. Sigalas, W. Zubrzycki, S. R. Kurtz, and J. Bur. A three-dimensional photonic crystal operating at infrared wavelengths. *Nature*, 394(6690):251–253, July 1998. doi: 10.1038/28343.

[32] M. J. A. de Dood, B. Gralak, A. Polman, and J. G. Fleming. Superstructure and finite-size effects in a si photonic woodpile crystal. *Physical Review B*, 67(3), January 2003. doi: 10.1103/physrevb.67.035322.

[33] T. G. Euser, A. J. Molenaar, J. G. Fleming, B. Gralak, A. Polman, and W. L. Vos. All-optical octave-broad ultrafast switching of si woodpile photonic band gap crystals. *Physical Review B*, 77(11), March 2008. doi: 10.1103/physrevb.77.115214.

[34] M. Adhikary, R. Uppu, C. A. M. Harteveld, D. A. Grishina, and W. L. Vos. Experimental probe of a complete 3d photonic band gap. *Optics Express*, 28(3):2683, January 2020. doi: 10.1364/oe.28.002683.

[35] Y. Baek and Y. Park. Intensity-based holographic imaging via space-domain kramers–kronig relations. *Nature Photonics*, 15(5):354–360, February 2021. doi: 10.1038/s41566-021-00760-8.